

Contribution of Radio Halos to the Foreground for SKA EoR Experiments

WEITIAN LI,¹ HAIGUANG XU,^{1, 2, 3} ZHIXIAN MA,⁴ DAN HU,¹ ZHENGHAO ZHU,¹ CHENXI SHAN,¹ JINGYING WANG,⁵ JUNHUA GU,⁶ XIAOLI LIAN,¹ QIAN ZHENG,⁷ JIE ZHU,⁴ AND XIANG-PING WU⁶

¹*School of Physics and Astronomy, Shanghai Jiao Tong University, 800 Dongchuan Road, Shanghai 200240, China*

²*Tsung-Dao Lee Institute, Shanghai Jiao Tong University, 800 Dongchuan Road, Shanghai 200240, China*

³*IFSA Collaborative Innovation Center, Shanghai Jiao Tong University, 800 Dongchuan Road, Shanghai 200240, China*

⁴*Department of Electronic Engineering, Shanghai Jiao Tong University, 800 Dongchuan Road, Shanghai 200240, China*

⁵*Department of Physics and Astronomy, University of the Western Cape, Cape Town 7535, South Africa*

⁶*National Astronomical Observatories, Chinese Academy of Sciences, 20A Datun Road, Beijing 100012, China*

⁷*Shanghai Astronomical Observatory, Chinese Academy of Sciences, 80 Nandan Road, Shanghai 200030, China*

(Received —; Revised —; Accepted —)

Submitted to ApJ

ABSTRACT

The overwhelming foreground contamination is one of the primary impediments to probing the EoR through measuring the redshifted 21 cm signal. Among various foreground components, radio halos are less studied and their impacts on the EoR observations are still poorly understood. In this work, we employ the Press-Schechter formalism, turbulence re-acceleration model, and the latest SKA1-Low layout configuration to simulate the SKA “observed” images of radio halos. We calculate the one-dimensional power spectra from simulated images and find that radio halos can be about 10^4 , 10^3 , and 10^2 times more luminous than the EoR signal on scales of $0.1 \text{ Mpc}^{-1} < k < 2 \text{ Mpc}^{-1}$ in the 120–128, 154–162, and 192–200 MHz bands, respectively. The two-dimensional power spectra obtained within the properly defined EoR windows, on the other hand, show that the power ratios of radio halos to the EoR signal on scales of $0.5 \text{ Mpc}^{-1} \lesssim k \lesssim 1 \text{ Mpc}^{-1}$ can still be about 10–20, 0.3–1, and

Corresponding author: Haiguang Xu
hgxu@sjtu.edu.cn
liweitianux@sjtu.edu.cn

0.1–0.8 in the three bands, when the 68 % errors caused by the uncertainties of the number density of bright radio halos are considered. In addition, we find that radio halos located inside the far side-lobes of the station beam can also impose strong contamination within the EoR window. In conclusion, we argue that radio halos are severe foreground sources and need serious treatments in future EoR experiments.

Keywords: dark ages, reionization, first stars — early universe — galaxies: clusters: intracluster medium — methods: data analysis — techniques: interferometric

1. INTRODUCTION

The Epoch of Reionization (EoR; $z \sim 6\text{--}15$) refers to a period of our Universe preceded by the Cosmic Dawn ($z \sim 15\text{--}30$) and the Dark Ages ($z \sim 30\text{--}200$) and is expected to last from about 300 million to about 1 billion years after the Big Bang (see [Koopmans et al. 2015](#), and references therein). During the EoR, the reionization of neutral hydrogen (HI), which was caused primarily by the ultra-violet and soft X-ray photons emitted from the first-generation celestial objects, efficiently surpassed the cooling of the gas. As a result, the majority of baryonic matter was again in a highly ionized state. Comparing with the observations of distant quasars and cosmic microwave background (CMB), which have provided some important but loose constraints on the reionization process (see [Fan et al. 2006](#), for a review), the 21 cm line emission of HI that is redshifted to frequencies below 200 MHz is regarded as the decisive probe to directly explore the EoR (see [Furlanetto et al. 2006](#); [Zaroubi 2013](#); [Furlanetto 2016](#), for reviews).

In order to probe the EoR, a number of radio interferometers working at the low-frequency radio bands ($\sim 50\text{--}200$ MHz) have been designed to target the redshifted 21 cm signal, among which there are the Square Kilometre Array (SKA; [Mellema et al. 2013](#); [Koopmans et al. 2015](#)), the Hydrogen Epoch of Reionization Array (HERA; [De-Boer et al. 2017](#)), and their pathfinders, such as the LOw Frequency ARray (LOFAR; [van Haarlem et al. 2013](#)), the Murchison Widefield Array (MWA; [Bowman et al. 2013](#); [Tingay et al. 2013](#)), the Precision Array for Probing the Epoch of Reionization (PAPER; [Parsons et al. 2010](#)), and the 21 CentiMeter Array (21CMA; [Zheng et al. 2016](#)). The challenges met in these experiments, however, are immense due to a variety of complicated instrumental effects, ionospheric distortions, radio frequency interference, and the strong celestial foreground contamination that overwhelms the redshifted 21 cm signal by about 4–5 orders of magnitude (see [Morales & Wyithe 2010](#), for a review).

Among various contaminating foreground components, the Galactic diffuse radiation (including both the synchrotron and free-free emissions) and extragalactic point sources are the most prominent and contribute the majority of the foreground contamination (e.g., [Shaver et al. 1999](#); [Di Matteo et al. 2004](#); [Gleser et al. 2008](#); [Liu](#)

& Tegmark 2012; Murray et al. 2017; Spinelli et al. 2018). At about 150 MHz, it is estimated that they may account for about 71% and 27% of the total foreground contamination, respectively (Shaver et al. 1999). Most of the remaining foreground contamination arises from the emission from the extragalactic diffuse sources that include the large-scale filaments embedded in cosmic webs (e.g., Vazza et al. 2015), the intergalactic medium located at cluster outskirts (e.g., Keshet et al. 2004), and the intracluster medium (ICM) of galaxy clusters (radio halos, relics, and mini-halos; e.g., Feretti et al. 2012). There are only limited observational evidences, especially in the low-frequency regime, to these diffuse sources. Among them, radio halos have gained relatively more observational constraints and theoretical understandings, which enable us to effectively evaluate their contamination on the EoR observations.

First discovered in the Coma cluster (Large et al. 1959), radio halos have been observed in about 80 merging galaxy clusters, exhibiting relatively regular morphologies and about Mpc spatial extensions. It should be noted that the angular sizes of radio halos appear to be several to tens of arcminutes, which coincide with those of the ionizing bubbles during the EoR. This, complemented with the potentially large number (several to tens of thousands in the whole sky) of radio halos to be revealed by the forthcoming low-frequency radio telescopes (e.g., Cassano et al. 2015), indicates that radio halos might be important contaminating foreground sources (e.g., Di Matteo et al. 2004; Gleser et al. 2008). As of today, however, only very few works have been dedicated to this topic and are all based on relatively straightforward modeling methods, such as using the 1.4 GHz radio flux function or radio–X-ray scaling relations that are barely constrained by the very limited observations (e.g., Gleser et al. 2008; Jelić et al. 2008). In this work, we focus on the radio halos and employ a sophisticated model to derive their low-frequency emission maps with the SKA1-Low’s instrumental effects incorporated. By making use of the power spectra and the EoR window, the contamination of radio halos on the EoR observations is quantitatively evaluated for both foreground removal and avoidance methods, which are the two major categories of methods that proposed to tackle the foreground contamination (see Chapman et al. 2016, and references therein).

This paper is prepared as follows. In Section 2 we simulate the low-frequency radio sky, among which a sophisticated simulation of radio halos is developed by employing the Press-Schechter formalism and turbulence re-acceleration model. In Section 3 we adopt the latest SKA1-Low layout configuration to incorporate the practical instrumental effects into the simulated sky maps. We briefly introduce the power spectra and the EoR window in Section 4 and then quantitatively evaluate the contamination caused by radio halos on the EoR measurements in Section 5. In Section 6, we discuss how the EoR detection is affected by radio halos due to the instrumental frequency artifacts and the far side-lobes of the station beam. Finally, we summarize our work in Section 7. Throughout this work we adopt a flat Λ CDM cosmology with $H_0 = 100 h = 71 \text{ km s}^{-1} \text{ Mpc}^{-1}$, $\Omega_m = 0.27$, $\Omega_\Lambda = 1 - \Omega_m = 0.73$,

Table 1. Simulation Parameters for the Three Bands

Frequency band (MHz)	120–128	154–162	192–200
Central frequency (f_c)	124 MHz	158 MHz	196 MHz
EoR redshift range	10.10–10.84	7.77–8.22	6.10–6.40
Bandwidth (B)		8 MHz	
Region size		$10^\circ \times 10^\circ$	
Image size		1800×1800	
Pixel size		$20''$	

$\Omega_b = 0.046$, $n_s = 0.96$, and $\sigma_8 = 0.81$. The quoted errors are at 68 % confidence level unless otherwise stated.

2. SIMULATION OF LOW-FREQUENCY RADIO SKY

Based on our previous works (Wang et al. 2010, 2013), we have developed the FG21sim¹ software to simulate the low-frequency radio sky by taking into account the contributions of our Galaxy, extragalactic point sources, and radio halos in galaxy clusters. We choose three representative frequency bands, namely 120–128, 154–162, and 192–200 MHz, and perform simulations for a sky patch of size $10^\circ \times 10^\circ$. The 8 MHz bandwidth is chosen to limit the effect of cosmological evolution of the EoR signal when calculating power spectra (e.g. Wyithe & Loeb 2004; Thyagarajan et al. 2013). The simulated sky maps are pixelized into 1800×1800 with a pixel size of $20''$. The simulation parameters are also listed in Table 1.

2.1. Radio Halos in Galaxy Clusters

As a significant improvement over our past works (Wang et al. 2010, 2013), we consider in detail the evolution of radio halos in galaxy clusters by employing the Press-Schechter formalism and turbulence re-acceleration model, in terms of which the relativistic electrons in the ICM are re-accelerated by the turbulence generated in merger events via the second-order Fermi process, and lose energies due to mechanisms including synchrotron radiation, inverse Compton scattering off the CMB photons, and Coulomb collisions with the thermal ICM (e.g., Cassano & Brunetti 2005; Brunetti & Lazarian 2007, 2011). For a galaxy cluster, we first employ the extended Press-Schechter theory to simulate its merging history, and then calculate the turbulent acceleration efficiency and duration for each merger event. By combining the effects of turbulent acceleration and energy loss, we obtain the temporal evolution of the relativistic electron spectrum, from which we calculate the synchrotron radiation of the radio halo.

2.1.1. Mass Function

¹ FG21sim: <https://github.com/liweitianux/fg21sim>

The Press-Schechter formalism was originally advanced as one of the standard method to predict the mass function of galaxy clusters and its evolution in the Universe (Press & Schechter 1974), and has been extended to combine with the cold dark matter (CDM) models (e.g., Bond et al. 1991; Lacey & Cole 1993). In this formalism, the number of galaxy clusters per unit comoving volume at redshift z in the mass range $[M, M + dM]$ is

$$n(M, z) dM = \sqrt{\frac{2}{\pi}} \frac{\langle \rho \rangle}{M} \frac{\delta_c(z)}{\sigma^2(M)} \left| \frac{d\sigma(M)}{dM} \right| \exp \left[-\frac{\delta_c^2(z)}{2\sigma^2(M)} \right] dM, \quad (1)$$

where M is the virial mass of galaxy clusters, $\langle \rho \rangle$ is the current mean density of the Universe, $\delta_c(z)$ is the critical linear overdensity for a region to collapse at redshift z [see Equation (B1)], and $\sigma(M)$ is the current root-mean-square (r.m.s.) density fluctuations within a sphere of mean mass M .

Considering the CDM model and the mass range covered by galaxy clusters, it is reasonable to adopt the following power-law distribution for the density perturbations (Sarazin 2002; Randall et al. 2002)

$$\sigma(M) = \sigma_8 \left(\frac{M}{M_8} \right)^{-\alpha}, \quad (2)$$

where σ_8 is the current r.m.s. density fluctuations on a scale of $8 h^{-1}$ Mpc, $M_8 = (4\pi/3)(8 h^{-1} \text{Mpc})^3 \langle \rho \rangle$ is the mass contained in a sphere of radius $8 h^{-1}$ Mpc, and the exponent $\alpha = (n + 3)/6$ with $n = -7/5$ (Randall et al. 2002) is related to the fluctuation pattern whose power spectrum varies with wavenumber k as k^n .

Using a minimum galaxy cluster mass of $M_{\min} = 10^{14} M_\odot$ and a maximum redshift cut at $z_{\max} = 4$, we apply Equation (1) to derive the total number of galaxy clusters in a given sky patch, together with the mass and redshift distributions. The galaxy cluster sample is then built by randomly drawing mass and redshift pairs $(M_{\text{sim}}, z_{\text{sim}})$ from these distributions.

2.1.2. *Merging History*

The extended Press-Schechter theory outlined in Lacey & Cole (1993) provides a way to describe the growth history of galaxy clusters in terms of the merger tree. In order to build the merger tree for a galaxy cluster, we start with its “current” mass M_{sim} and redshift z_{sim} obtained in Section 2.1.1, and trace its growth history back in time by running Monte Carlo simulations to randomly determine the mass change ΔM at each step, which may be regarded either as a merger event (if $\Delta M > \Delta M_c$) or as an accretion event (if $\Delta M \leq \Delta M_c$). Since radio halos are usually associated with major mergers, we choose $\Delta M_c = 10^{13} M_\odot$ (e.g., Cassano & Brunetti 2005).

We assume that during each growth step the cluster mass increases from M_1 at time t_1 to M_2 at a later time t_2 ($> t_1$). Given M_2 and t_2 , the conditional probability of the cluster had a progenitor of mass in the range $[M_1, M_1 + dM_1]$ at an earlier time

t_1 can be expressed as

$$\Pr(M_1, t_1 | M_2, t_2) dM_1 = \frac{1}{\sqrt{2\pi}} \frac{M_2}{M_1} \frac{\delta_{c1} - \delta_{c2}}{(\sigma_1^2 - \sigma_2^2)^{3/2}} \left| \frac{d\sigma_1^2}{dM_1} \right| \exp \left[-\frac{(\delta_{c1} - \delta_{c2})^2}{2(\sigma_1^2 - \sigma_2^2)} \right] dM_1, \quad (3)$$

where $\delta_{ci} \equiv \delta_c(t_i)$, $\sigma_i \equiv \sigma(M_i)$, and $i = 1, 2$ are used to denote parameters defined at time t_1 and t_2 , respectively (Lacey & Cole 1993; Randall et al. 2002). By further introducing $S \equiv \sigma^2(M)$ and $\omega \equiv \delta_c(t)$, this equation reduces to

$$\Pr(\Delta S, \Delta \omega) d\Delta S = \frac{1}{\sqrt{2\pi}} \frac{\Delta \omega}{(\Delta S)^{3/2}} \exp \left[-\frac{(\Delta \omega)^2}{2\Delta S} \right] d\Delta S. \quad (4)$$

In order to resolve mergers with a mass change $\Delta M_c \ll M$ during the backward tracing of a galaxy cluster, a time step Δt (i.e., $\Delta \omega$) that satisfies

$$\Delta \omega \lesssim \Delta \omega_{\max} = \left[S \left| \frac{d \ln \sigma^2}{d \ln M} \right| \left(\frac{\Delta M_c}{M} \right) \right]^{1/2} \quad (5)$$

is required (Lacey & Cole 1993), and we adopt an adaptive step of $\Delta \omega = \Delta \omega_{\max}/2$ (Randall et al. 2002). At a certain step when $\Delta \omega$ is given, the mass change ΔS can be randomly drawn from the following cumulative probability distribution of sub-cluster masses

$$\Pr(<\Delta S, \Delta \omega) = \int_0^{\Delta S} \Pr(\Delta S', \Delta \omega) d\Delta S' = \text{erfc} \left(\frac{\Delta \omega}{\sqrt{2\Delta S}} \right), \quad (6)$$

where $\text{erfc}(x) = 1 - \text{erf}(x)$ is the complementary error function, and the cluster's progenitor mass M_1 is then obtained as $S_1 = S_2 + \Delta S$.

Given that observable radio halos are regarded to be associated with recent (in observer's frame) major mergers and have typical lifetimes $\tau_{\text{halo}} \lesssim 1$ Gyr at 1.4 GHz (e.g., Brunetti et al. 2009; Cassano et al. 2016), we trace the merging history of each galaxy cluster by a maximum backward time of 3 Gyr from its “current” age t_{sim} (corresponding to z_{sim}). For each built merger tree, we extract the information of all the mergers associated with the main cluster to carry out the simulation of radio halos.

2.1.3. Evolution of Radio Halos

According to the re-acceleration model, there exists a population of primary (or fossil) high-energy electrons, which permeate the ICM and are thought to be injected by multiple processes, such as active galactic nucleus (AGN) activities and star formations (see Blasi et al. 2007, for a review). When a cluster experiences a major merger, the turbulence is generated throughout the ICM and can accelerate the primary electrons to be highly relativistic, resulting in the observed radio halo. On the other hand, relativistic electrons in the ICM lose energy via mechanisms that include synchrotron radiation, inverse Compton scattering off the CMB photons, and Coulomb collisions (Sarazin 1999). For a population of electrons with isotropic energy

distribution, the temporal evolution of the number density distribution $n(\gamma, t)$ is governed by the following Fokker-Planck diffusion-advection equation (Eilek & Hughes 1991; Schlickeiser 2002)

$$\frac{\partial n(\gamma, t)}{\partial t} = \frac{\partial}{\partial \gamma} \left[n(\gamma, t) \left(\left| \frac{d\gamma}{dt} \right| - \frac{2}{\gamma} D_{\gamma\gamma}(\gamma, t) \right) \right] + \frac{\partial}{\partial \gamma} \left[D_{\gamma\gamma} \frac{\partial n(\gamma, t)}{\partial \gamma} \right] + Q_e(\gamma, t), \quad (7)$$

where γ is the Lorentz factor of electrons, $D_{\gamma\gamma}(\gamma, t)$ is the diffusion coefficient describing the interactions between the turbulence and electrons, $|d\gamma/dt|$ is the energy loss rate, and $Q_e(\gamma, t)$ describes the electron injection.

a. Thermal Electrons

The number density of thermal electrons n_{th} in the ICM can be calculated as

$$n_{\text{th}} \simeq \frac{3 f_b M_{\text{vir}}}{4\pi \mu m_u r_{\text{vir}}^3}, \quad (8)$$

where $f_b \simeq \Omega_b/\Omega_m$ is the mean baryon fraction assumed for galaxy clusters, M_{vir} is the cluster's virial mass, r_{vir} is the virial radius [see Equation (B5)], $\mu \simeq 0.6$ is the mean molecular weight (e.g., Ettori et al. 2013), and m_u is the atomic mass unit. Therefore, the corresponding thermal energy density ϵ_{th} of the ICM is given by

$$\epsilon_{\text{th}} = \frac{3}{2} n_{\text{th}} k_B T_{\text{cl}}, \quad (9)$$

where the cluster's mean temperature is approximated as the virial temperature, i.e., $k_B T_{\text{cl}} \simeq k_B T_{\text{vir}} = GM_{\text{vir}}\mu m_u/(2r_{\text{vir}})$.

b. Electron Injection

As primary electrons are continuously injected into the ICM via multiple processes, it is reasonable to assume an average injection rate and a power-law spectrum for the electron injection process (e.g., Cassano & Brunetti 2005; Donnert & Brunetti 2014)

$$Q_e(\gamma, t) \simeq Q_e(\gamma) = K_e \gamma^{-s}, \quad (10)$$

where $s = 2.3$ is the adopted spectral index (e.g., Sarazin 1999). Moreover, the total energy of the injected electrons can be assumed to account for a fraction (η_e) of the ICM's total thermal energy (Cassano & Brunetti 2005), i.e.,

$$\epsilon_e \tau_{\text{cl}} \int_{\gamma_{\min}}^{\gamma_{\max}} Q_e(\gamma') \gamma' d\gamma' = \eta_e \epsilon_{\text{th}}, \quad (11)$$

where $\tau_{\text{cl}} \simeq t_{\text{sim}}$ is the cluster's age at its “current” redshift z_{sim} , and $\epsilon_e = m_e c^2$ is the electron's rest energy. Given $\gamma_{\min} \ll \gamma_{\max}$, the injection rate K_e is derived to be

$$K_e \simeq \frac{(s-2) \eta_e \epsilon_{\text{th}}}{\epsilon_e \tau_{\text{cl}}} \gamma_{\min}^{s-2}. \quad (12)$$

c. Initial Electron Spectrum

To determine the initial electron spectrum $n_e(\gamma, t_0)$, which will be used to solve Equation (7), we evolve the accumulated electron spectrum $n'_e(\gamma) = Q_e(\gamma) \tau_0$ for 1 Gyr by applying the same Fokker-Planck equation with the turbulent acceleration turned off (e.g., Brunetti & Lazarian 2007), where τ_0 is the cluster's age in the beginning of the first merger and is approximated as the starting time of the first merger.

d. Turbulent Acceleration

The details of interactions between the turbulence and both thermal and relativistic particles are complicated and still poorly understood. Among several particle acceleration mechanisms that can be potentially triggered by the turbulence, the most important one is the transit time damping process, i.e., the turbulence dissipates its energy and accelerates particles by interacting with the relativistic particles (e.g., cosmic rays) in the ICM (Brunetti & Lazarian 2007, 2011, and references therein). The associated diffusion coefficient is given as (Pinzke et al. 2017; Miniati 2015)

$$D_{\gamma\gamma} = \gamma^2 \frac{4\pi\zeta}{X_{\text{cr}} L_{\text{turb}}} \frac{\langle (\delta v_t)^2 \rangle^2}{c_s^3}, \quad (13)$$

where $\zeta \sim 0.1\text{--}0.3$ is an efficiency factor characterizing the plasma instabilities (e.g., due to spatial or temporal intermittency), $X_{\text{cr}} = \epsilon_{\text{cr}}/\epsilon_{\text{th}} \sim 1\%$ is the relative energy density of cosmic rays with respect to the thermal ICM, $L_{\text{turb}} \simeq r_{\text{vir}}/3$ is the turbulence injection scale (Miniati 2015), $\langle (\delta v_t)^2 \rangle$ is the turbulence velocity dispersion, and $c_s = \sqrt{\gamma_{\text{gas}} k_B T_{\text{cl}} / (\mu m_u)}$ is the sound speed in the ICM with $\gamma_{\text{gas}} = 5/3$ being the adiabatic index of ideal monatomic gas.

In order to estimate the velocity dispersion of the turbulence, we assume that a fraction (η_{turb}) of the kinetic energy carried by the merger is transferred into turbulent waves, i.e.,

$$E_{\text{turb}} = \frac{1}{2} M_{\text{turb}}^b \langle (\delta v_t)^2 \rangle = \eta_{\text{turb}} E_{\text{merger}}, \quad (14)$$

where M_{turb}^b is the baryon mass enclosed in the turbulent region (i.e., within radius of L_{turb}), and E_{merger} is merger's kinetic energy, which can be approximated as the potential energy released from the infalling sub-cluster

$$E_{\text{merger}} \simeq \frac{1}{2} f_b M_{\text{vir,s}} v_{\text{vir}}^2 \simeq \frac{1}{2} f_b M_{\text{vir,s}} \frac{GM_{\text{vir,m}}}{r_{\text{vir,m}}^2}, \quad (15)$$

where $M_{\text{vir,m}}$ and $r_{\text{vir,m}}$ are the virial mass and radius of the main cluster, respectively, and $M_{\text{vir,s}}$ is the virial mass of the sub-cluster. By adopting the NFW density profile (Navarro et al. 1997), the distribution of mass within a radius of $s r_{\text{vir}}$ (s is the normalized radius in units of the virial radius) in fraction of the virial mass is

$$f_{\text{nfw}}(s) = \frac{M(< s r_{\text{vir}})}{M_{\text{vir}}} = \frac{\ln(1 + cs) - cs/(1 + cs)}{\ln(1 + c) - c/(1 + c)}, \quad (16)$$

where $c \sim 5$ is the concentration parameter for clusters (Lokas & Mamon 2001). Therefore we have

$$M_{\text{turb}}^b = f_b M_{\text{merged}}(< L_{\text{turb}}) = f_b f_{\text{nfw}}(1/3)(M_{\text{vir,m}} + M_{\text{vir,s}}). \quad (17)$$

By substituting Equations (15) and (17) into Equation (14), we obtain the turbulence velocity dispersion as

$$\langle (\delta v_t)^2 \rangle = \frac{\eta_{\text{turb}}}{f_{\text{nfw}}(1/3)} \frac{M_{\text{vir,s}}}{M_{\text{vir,m}} + M_{\text{vir,s}}} \frac{GM_{\text{vir,m}}}{r_{\text{vir,m}}^2}. \quad (18)$$

Generally, the turbulence generated during major mergers is subsonic with a Mach number of $\mathcal{M}_{\text{turb}} = \sqrt{\langle (\delta v_t)^2 \rangle} / c_s \sim 0.2\text{--}0.5$. The acceleration efficiency can be described by the systematic acceleration timescale (i.e., the reciprocal of the acceleration rate; e.g., Brunetti & Lazarian 2011) $\tau_{\text{acc}} = \gamma^2 / (4D_{\gamma\gamma}) \sim 0.1$ Gyr, suggesting that the turbulent acceleration is a moderately efficient mechanism to accelerate the relativistic electrons in the ICM and may be used to explain the origin of radio halos.

e. Acceleration Periods

The whole merger process may last for 2–3 Gyr (e.g., Tormen et al. 2004; Cassano et al. 2016); however, the period τ_{turb} during which the turbulence is intense enough to be able to effectively accelerate particles is relatively short: $\tau_{\text{turb}} \simeq 2L_{\text{turb}}/v_{\text{imp}}$, where v_{imp} is the relative impact velocity between the merging clusters (Miniati 2015). Starting from a sufficiently large distance with zero velocity, the relative impact velocity of two merging clusters with masses $M_{\text{vir,m}}$ and $M_{\text{vir,s}}$ is given by (Sarazin 2002; Cassano & Brunetti 2005)

$$v_{\text{imp}} \simeq \left[\frac{2G(M_{\text{vir,m}} + M_{\text{vir,s}})}{r_{\text{vir,m}}} \left(1 - \frac{1}{\eta_v} \right) \right]^{1/2}, \quad (19)$$

where $\eta_v \simeq 4(1 + M_{\text{vir,s}}/M_{\text{vir,m}})^{1/3}$. Based on these, we estimate that major mergers generally have an effective turbulent acceleration duration of $\tau_{\text{turb}} \sim 0.5$ Gyr.

For each merger event $(M_{\text{vir,m}}^{(i)}, M_{\text{vir,s}}^{(i)}, t_{\text{merger}}^{(i)})$ as simulated in Section 2.1.2 for a galaxy cluster, where $t_{\text{merger}}^{(i)}$ denotes the starting time of the i -th merger event, we calculate the corresponding turbulent acceleration duration $\tau_{\text{turb}}^{(i)}$. We then solve Equation (7) by taking into account both turbulent acceleration and energy losses during the period $[t_{\text{merger}}^{(i)}, t_{\text{merger}}^{(i)} + \tau_{\text{turb}}^{(i)}]$, while there is no turbulent acceleration at other times.

f. Energy Losses

Among the several mechanisms through which the relativistic electrons in the ICM can lose energy, we take into account the following three major mechanisms in this work (Sarazin 1999). The first one is the inverse Compton scattering off the CMB photons, the energy loss rate of which is

$$\left(\frac{d\gamma}{dt} \right)_{\text{IC}} = -4.32 \times 10^{-4} \gamma^2 (1+z)^4 \quad [\text{Gyr}^{-1}]. \quad (20)$$

Secondly, with the μG -level magnetic field permeating the ICM, relativistic electrons will produce synchrotron radiation and lose energy at a rate of

$$\left(\frac{d\gamma}{dt} \right)_{\text{syn}} = -4.10 \times 10^{-5} \gamma^2 \left(\frac{B}{1 \mu\text{G}} \right)^2 \quad [\text{Gyr}^{-1}], \quad (21)$$

where B is the mean magnetic field strength. We assume that the magnetic field is uniform and its energy density is a fraction of the thermal energy density, i.e., $u_B = B^2/(8\pi) = \eta_B \epsilon_{\text{th}}$, where η_B is the energy density ratio between the magnetic field and the thermal ICM (e.g., Böhringer et al. 2016).

The last mechanism considered is that relativistic electrons interact with the thermal electrons via Coulomb collisions, the energy loss rate of which is

$$\left(\frac{d\gamma}{dt} \right)_{\text{Coul}} = -3.79 \times 10^4 \left(\frac{n_{\text{th}}}{1 \text{ cm}^{-3}} \right) \left[1 + \frac{1}{75} \ln \left(\gamma \frac{n_{\text{th}}}{1 \text{ cm}^{-3}} \right) \right] \text{ [Gyr}^{-1}\text{].} \quad (22)$$

The inverse Compton scattering and synchrotron radiation dominate the energy losses at the high-energy regime ($\gamma \gtrsim 1000$), while Coulomb collisions are the main energy-loss mechanism for electrons with lower energies ($\gamma \lesssim 100$). Therefore, electrons with intermediate energies (e.g., $\gamma \sim 300$) have a long lifetime (~ 3 Gyr) and can accumulate in the ICM as the cluster grows (Sarazin 1999).

g. Numerical Method

To derive the “current” electron spectrum $n_e(\gamma, t_{\text{sim}})$ from the initial spectrum $n_e(\gamma, t_0)$, we employ an efficient numerical method proposed by Chang & Cooper (1970) to solve the Fokker-Planck equation under the no-flux boundary condition (Park & Petrosian 1996). To avoid the unphysical pile-up of electrons around the lower boundary caused by the boundary condition, we define a “buffer” region below γ_{buf} , within which the spectral data are replaced by extrapolating the data above γ_{buf} as a power-law spectrum (Donnert & Brunetti 2014). We adopt a logarithmic grid for $\gamma \in [1, 10^5]$ with 200 cells, and let the buffer region span 10 cells.

h. Image Generation

After deriving the “current” electron spectrum $n_e(\gamma, t_{\text{sim}})$, the synchrotron emissivity at frequency ν is given by (Rybicki & Lightman 1979)

$$J_{\text{syn}}(\nu) = \frac{\sqrt{3} e^3 B}{m_e c^2} \int_{\gamma_{\text{min}}}^{\gamma_{\text{max}}} \int_0^{\pi/2} n_e(\gamma, t_{\text{sim}}) F(\nu/\nu_c) \sin^2 \theta d\theta d\gamma, \quad (23)$$

where θ is the pitch angle of electrons, and $F(\nu/\nu_c) = (\nu/\nu_c) \int_{\nu/\nu_c}^{\infty} K_{5/3}(x) dx$ is the synchrotron kernel with $K_{5/3}(x)$ being the modified Bessel function of 5/3 order, $\nu_c = (3/2) \gamma^2 \nu_L \sin \theta = 3eB\gamma^2 \sin \theta / (4\pi m_e c)$ the electron’s critical frequency. The radio halo is assumed to be the same size as the turbulent region (Vazza et al. 2011), i.e., $r_{\text{halo}} \simeq L_{\text{turb}} \simeq r_{\text{vir}}/3$, therefore its radio power at a certain frequency is

$$P(\nu) = \frac{4\pi}{3} r_{\text{halo}}^3 J_{\text{syn}}(\nu), \quad (24)$$

and its flux density at the same frequency is

$$S(\nu) = \frac{(1+z_{\text{sim}}) P(\nu(1+z_{\text{sim}}))}{4\pi D_L^2(z_{\text{sim}})}, \quad (25)$$

where $D_L(z_{\text{sim}})$ is the luminosity distance to the halo at redshift z_{sim} , and the factor $(1 + z_{\text{sim}})$ accounts for the K correction (e.g., Hogg 1999).

To generate the image for the simulated radio halos, we adopt an exponential profile for the azimuthally averaged brightness distribution (Murgia et al. 2009):

$$I_\nu(\theta) = I_{\nu,0} \exp(-3\theta/\theta_{\text{halo}}), \quad (26)$$

where $\theta = r/D_A(z_{\text{sim}})$ is the angular radius from the halo center with $D_A(z_{\text{sim}})$ being the angular diameter distance to the halo, and $I_{\nu,0} = 9S(\nu)/(2\pi\theta_{\text{halo}}^2)$ is the central brightness.

i. Parameters Tuning

Our model has the following 5 parameters: (1) fraction of the merger energy transferred into the turbulence: $\eta_{\text{turb}} \sim 10\%$; (2) relative energy density of the magnetic field: $\eta_B \sim 0.1\%$; (3) ratio of the total energy of injected electrons to the total thermal energy: $\eta_e \sim 0.1\%$; (4) efficiency of the ICM plasma instabilities: $\zeta \sim 0.1$; (5) relative energy density in the cosmic rays: $X_{\text{cr}} \sim 1.5\%$. Although all of them have reasonable constraints from either observation or simulation studies, it is essential to further tune them in order to achieve better agreement with the observations. To this end, we have collected all currently observed radio halos (Table A1 in Appendix A; 71 identified halos and 9 candidates; as of 2018 January), and compare the 1.4 GHz all-sky integrated flux function between our simulated radio halos and the observations. We have explored various parameter configurations, and for each configuration we have repeated the simulation for 500 times in order to take into account the distribution variations of bright radio halos across the sky. Considering that the current observations are far from complete, especially in the low-flux end, our strategy is requiring that the integrated flux function of simulated radio halos agrees with the observed one in the high-flux end within error bars. Consequently, we have chosen a set of model parameters with $\eta_{\text{turb}} = 10\%$, $\eta_B = 0.1\%$, $\eta_e = 0.3\%$, $\zeta = 0.1$, and $X_{\text{cr}} = 1.5\%$. A comparison between the 1.4 GHz all-sky integrated flux functions of radio halos obtained in observations and simulations is shown in Figure 1, where we also plot the 158 MHz all-sky integrated flux function for the simulated radio halos, which shows that radio halos are much brighter at lower frequencies.

In order to describe the uncertainty of the number density of bright radio halos across the sky, we repeat the simulation of radio halos for 100 times. The medians and the corresponding 68% errors² of the r.m.s. brightness temperature are $(6.95^{+21.0}_{-5.04}) \times 10^3$ mK, $(2.75^{+10.4}_{-1.97}) \times 10^3$ mK, and $(1.24^{+4.86}_{-0.92}) \times 10^3$ mK at 124, 158, and 196 MHz, respectively (Table 2; see also Figure 2 for an example map of the simulated radio halos at 158 MHz).

2.2. Other Foreground Components

² The 68% error is derived from the 16th and 84th percentiles because they are more robust than the mean and standard deviation for data with large dispersion.

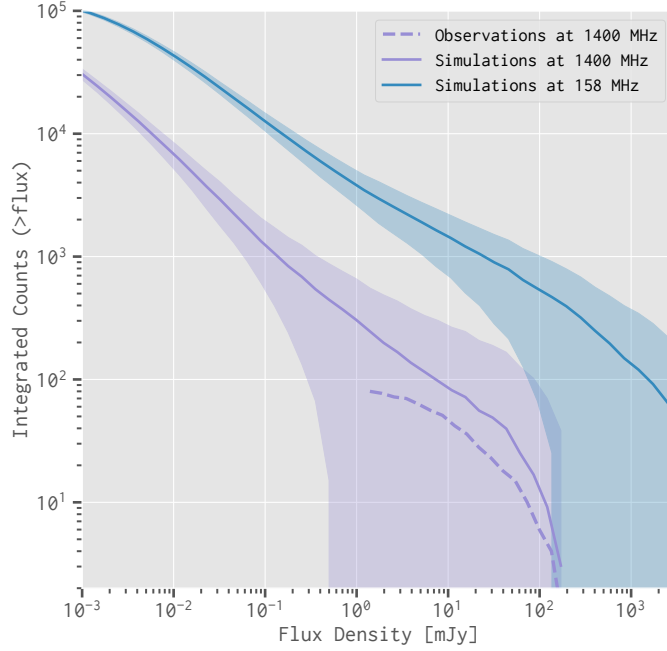


Figure 1. The 1.4 GHz all-sky integrated flux function comparison between the observed (the dashed purple line) and simulated (the solid purple line) radio halos. The 158 MHz all-sky integrated flux function for the simulated halos is also plotted in the solid blue line. The shaded regions show the 68 % errors of the simulated radio halos derived from the 500 simulation runs.

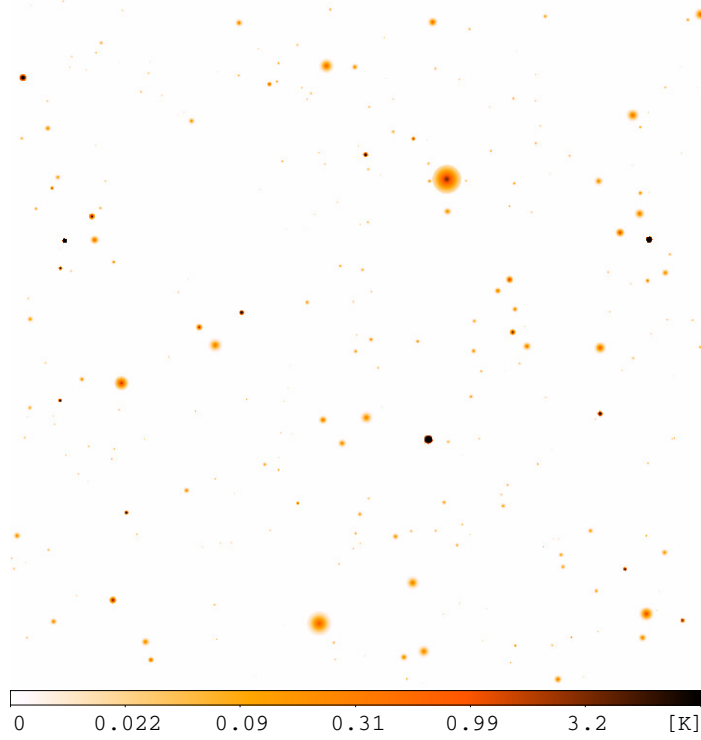


Figure 2. An example from the 100 simulation runs showing the simulated radio halos at 158 MHz. The sky region size is $10^\circ \times 10^\circ$, and the color bar is in units of K.

Table 2. The r.m.s. Brightness Temperatures of the Foreground Components and the EoR Signal (unit: mK)

Component	124 MHz	158 MHz	196 MHz
Radio halos (100 simulations)	$(6.95^{+21.0}_{-5.04}) \times 10^3$	$(2.75^{+10.4}_{-1.97}) \times 10^3$	$(1.24^{+4.86}_{-0.92}) \times 10^3$
Galactic synchrotron	4.74×10^5	2.52×10^5	1.43×10^5
Galactic free-free	330	200	130
Extragalactic point sources	2.97×10^8	5.90×10^7	1.39×10^7
EoR signal	15.1	11.3	3.77

Following our previous work (Wang et al. 2010), we have also simulated several other foreground components, including the Galactic synchrotron and free-free emissions as well as the extragalactic point sources, in order to carry out comparisons of power spectra between radio halos and other foreground components as an effort to better characterize the contribution of radio halos to the low-frequency radio sky.

The Galactic synchrotron map is simulated by extrapolating the Haslam 408 MHz all-sky map as the template to lower frequencies with a power-law spectrum. We make use of the high-resolution version ($N_{\text{side}} = 2048$, pixel size $\sim 1.72'$) of the Haslam 408 MHz map³, which was reprocessed by Remazeilles et al. (2015) using significantly better instrument calibration and more accurate subtraction of extragalactic sources. We also use the all-sky synchrotron spectral index map made by Giardino et al. (2002) to account for the index variation with sky positions. The Galactic free-free emission is deduced from the H α survey data (Finkbeiner 2003), which is corrected for dust absorption, by employing the tight relation between the H α and free-free emissions due to their common origins (see Dickinson et al. 2003, and references therein). Since the Galactic diffuse emissions vary remarkably across the sky, we simulate them at position of (R.A., Dec.) = (0°, −27°), which locates at a high galactic latitude ($b = -78.5^\circ$) and is expected to be an appropriate choice for this study (see also Section 3).

The extragalactic point sources are simulated by taking into account the following 5 types of sources: (1) star-forming and starburst galaxies, (2) radio-quiet AGNs, (3) Fanaroff-Riley type I and type II AGNs, (4) GHz-peaked spectrum AGNs, and (5) compact steep spectrum AGNs. We simulate the former three types of sources by leveraging the simulation results made by Wilman et al. (2008), and simulate the latter two types by employing their corresponding luminosity functions and spectral models. More details can be found in Wang et al. (2010) and references therein.

³ The reprocessed Haslam 408 MHz map: http://www.jb.man.ac.uk/research/cosmos/haslam_map/.

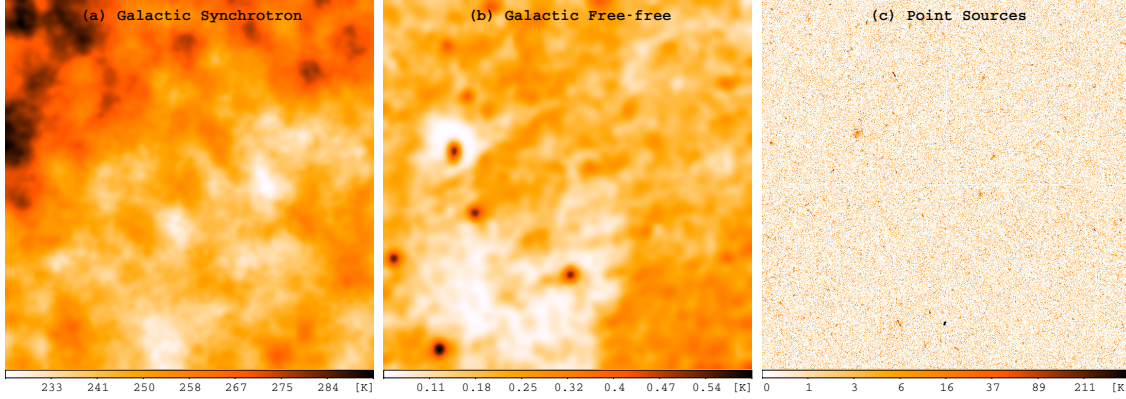


Figure 3. The sky maps of (a) the Galactic synchrotron emission, (b) the Galactic free-free emission, and (c) the extragalactic point sources at 158 MHz. All the maps cover sky region of size $10^\circ \times 10^\circ$, and have color bars in units of K.

The r.m.s. brightness temperatures of the Galactic synchrotron emission, Galactic free-free emission, and extragalactic point sources are listed in Table 2, and example maps simulated at 158 MHz for these components are shown in Figure 3.

2.3. *The EoR Signal*

The sky maps of the EoR signal are created using the 2016 data release from the Evolution Of 21 cm Structure project⁴, which has made use of the 21cmFAST to simulate the cosmic reionization process from redshift 86.5 to 5.0 inside a large cube that is 1.6 comoving Gpc (1024 cells) along each side (Mesinger et al. 2016). We extract the image slices at needed frequencies (i.e., redshifts) from the light-cone cubes of the recommended “faint galaxies” case, and then tile and re-scale them to have the same sky coverage and pixel size as our foreground maps. Figure 4 shows the r.m.s. brightness temperatures of the EoR signal among 120–200 MHz ($z = 6.1\text{--}10.8$). The corresponding r.m.s. brightness temperatures at the central frequencies of the three adopted bands and the map of the EoR signal obtained at 158 MHz are given in Table 2 and Figure 5, respectively.

3. SIMULATION OF SKA OBSERVATIONS

In order to properly evaluate the contamination of radio halos on the EoR observations, it is essential to take account of the practical instrumental effects of radio interferometers. Therefore, we employ the latest SKA1-Low layout configuration⁵ to simulate the SKA observations of the above simulated sky maps. According to this layout configuration, the SKA1-Low interferometer consists of 512 stations, with 224 of them randomly distributed within the “core” of 1000 m in diameter, while the remaining stations are grouped into “clusters” and placed on 3 spiral arms extending up to a radius of \sim 35 km. Each station has 256 antennas randomly distributed with

⁴ Evolution Of 21 cm Structure project: <http://homepage.sns.it/mesinger/EOS.html>

⁵ SKA1-Low Configuration Coordinates: https://astronomers.skatelescope.org/wp-content/uploads/2016/09/SKA-TEL-SKO-0000422_02_SKA1_LowConfigurationCoordinates-1.pdf (released on 2016 May 21)

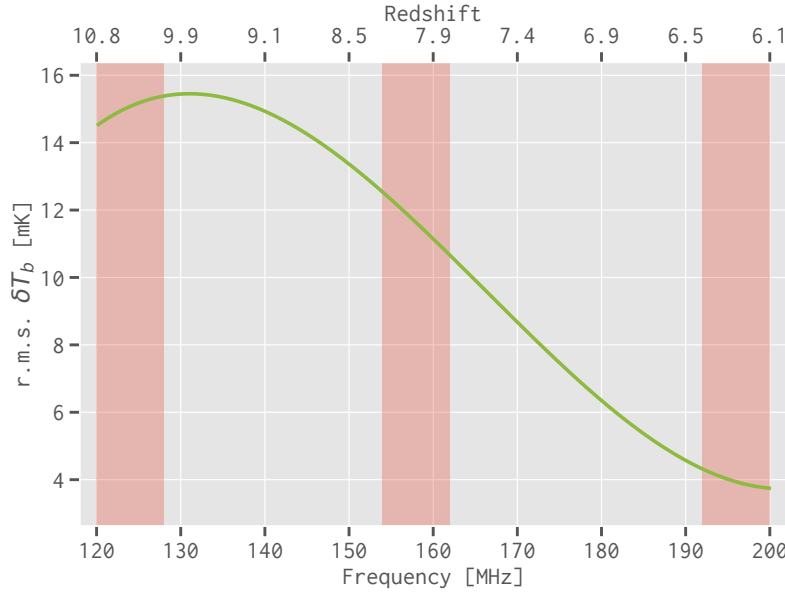


Figure 4. The r.m.s. brightness temperatures of the EoR signal (the solid green line) within 120–200 MHz ($z = 6.1$ – 10.8). The red shaded regions mark the 120–128, 154–162, and 192–200 MHz frequency bands adopted in this work.

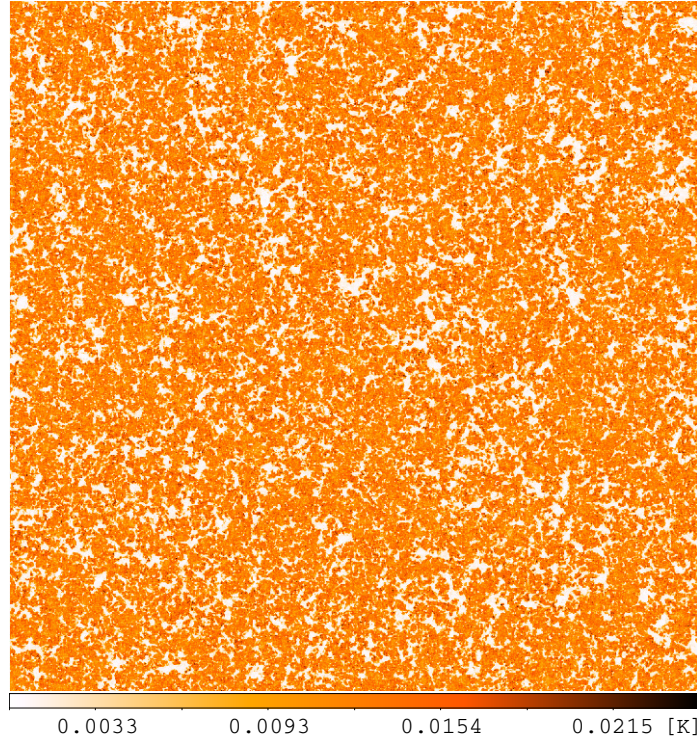


Figure 5. The sky map of the EoR signal at 158 MHz. The sky region size is $10^\circ \times 10^\circ$, and the color bar is in units of K.

a minimum separation of $d_{\min} = 1.5$ m inside a circular region of 35 m in diameter (e.g., Mort et al. 2017).

The 8 MHz bandwidth of each frequency band is divided into 51 channels for a frequency resolution of 160 kHz. For each component, we simulate the input sky maps at every frequency channel, and then use the `OSKAR`⁶ simulator (Mort et al. 2010) to perform observations for 6 hr. The input sky maps are centered at sky position of (R.A., Dec.) = (0°, −27°), which passes through the zenith of the SKA1-Low telescope and is an ideal choice for the simulation of SKA observations. The simulated visibility data are imaged through the `WSClean`⁷ imager (Offringa et al. 2014) using Briggs’ weighting with a robustness of zero (Briggs 1995), and the created images are cropped to keep only the central regions because the marginal regions suffer from the problem of insufficient CLEAN. As the telescope’s field of view (FoV) is inversely proportional to the observing frequency, we choose to keep the central 6° × 6°, 5° × 5°, and 4° × 4° regions in the 120–128, 154–162, and 192–200 MHz frequency bands, respectively.

The Galactic synchrotron and free-free emissions are combined for the simulated observations because they have similar diffuse features. Similar to the real-time peeling of the brightest point sources in practical data analysis pipelines (e.g., Mitchell et al. 2008; Intema et al. 2009; Mort et al. 2017), we assume that the point sources with a 158 MHz flux density $S_{158} > 50$ mJy are removed (e.g., Pindor et al. 2011). The r.m.s. brightness temperatures of extragalactic point sources are hence significantly reduced to be about (22.5, 9.81, and 4.75) × 10⁴ mK at 124, 158, and 196 MHz, respectively. In addition, we create the foreground image cubes in each frequency band using the CLEAN algorithm with joined-channel deconvolution in order to ensure the spectral smoothness (Offringa & Smirnov 2017), which is crucial to extract the faint EoR signal in the presence of overwhelming foreground contamination. For the EoR signal, we directly use the dirty images because the CLEAN algorithm is not well applicable to such faint and diffuse emissions. Hence we obtain the SKA “observed” image cubes of the EoR signal, radio halos, the Galactic diffuse emission (with synchrotron and free-free emissions combined), and the extragalactic point sources (with the brightest ones removed) in the 120–128, 154–162, and 192–200 MHz frequency bands.

4. POWER SPECTRA AND EOR WINDOW

In order to characterize the contamination of radio halos on the EoR observations in terms of both foreground removal and avoidance methods, we utilize the power spectra and EoR window to compare the powers of radio halos with the EoR signal as well as other foreground components. The redshifted 21 cm signal expected to be observed at different frequencies represents a three-dimensional (3D) data cube, where the two spatial dimensions describe the transverse distances across the sky and the frequency dimension maps to the line-of-sight distance. Within a limited redshift range (e.g., $\Delta z \sim 0.5$, corresponding to a frequency bandwidth of ∼8 MHz

⁶ OSKAR: <https://github.com/OxfordSKA/OSKAR> (version 2.7.0)

⁷ WSClean: <https://sourceforge.net/p/wsclean> (version 2.5)

at 158 MHz) during the EoR, the evolution effect of the Universe is minor and the HI distribution is believed to be isotropic. The corresponding 3D power spectrum $P(k_x, k_y, k_z)$ of the EoR signal should have spherical symmetry and can be averaged in spherical shells of radii k , yielding the one-dimensional (1D) power spectrum $P(k)$, which effectively increases the signal-to-noise ratio compared to direct imaging observations (Morales & Hewitt 2004; Morales et al. 2006; Datta et al. 2010). The “dimensionless” variant of the 1D power spectrum $\Delta^2(k) = P(k)k^3/(2\pi^2)$ is more commonly used in the literature. To suppress the significant side-lobes in the Fourier transform caused by the sharp discontinuities at the ends of the finite frequency band, we apply the Blackman-Nuttall window function to the frequency dimension before calculating the power spectra (e.g., Trott & Tingay 2015; Chapman et al. 2016).

Since the two angular dimensions and the frequency dimension of the image cubes of foreground continuum emissions are independent, which is different from the image cube of the redshifted 21 cm signal, it is appropriate to average the 3D power spectrum $P(k_x, k_y, k_z)$ over angular annuli of radii $k_\perp \equiv \sqrt{k_x^2 + k_y^2}$ for each line-of-sight plane $k_\parallel \equiv k_z$, which yields the two-dimensional (2D) power spectrum $P(k_\perp, k_\parallel)$. In the (k_\perp, k_\parallel) plane, the spectral-smooth foreground emissions are supposed to reside in the low- k_\parallel region, although complicated instrumental and observational effects (e.g., chromatic primary beams, calibration errors) can throw some of the foreground contamination from the purely angular (k_\perp) modes into the line-of-sight (k_\parallel) dimension (i.e., mode mixing), which results in an expanded wedge-like contamination region at the bottom-right in the (k_\perp, k_\parallel) plane (“foreground wedge”; Datta et al. 2010; Morales et al. 2012; Liu et al. 2014). The region almost free of the foreground contamination, namely the “EoR window,” is preserved at the top-left in the (k_\perp, k_\parallel) plane and can be described with (Thyagarajan et al. 2013)

$$k_\parallel \geq \frac{H(z)D_M(z)}{c(1+z)} \left[k_\perp \sin \Theta + \frac{e}{B} \frac{2\pi f_{21}}{(1+z)D_M(z)} \right], \quad (27)$$

where c is the speed of light, $B = 8$ MHz is the frequency bandwidth of the image cube, $f_{21} = 1420.4$ MHz is the rest-frame frequency of the 21 cm line, $z = f_{21}/f_c - 1$ is the signal redshift corresponding to the central frequency (f_c) of the image cube, $H(z)$ is the Hubble parameter at redshift z [see Equation (B4)], $D_M(z)$ is the transverse comoving distance, e denotes the number of characteristic convolution widths ($\propto B^{-1}$) for the spillover region caused by the variations in instrumental frequency response, and Θ is the angular distance of foreground sources from the field center.

5. RESULTS

We evaluate the contamination of radio halos on the EoR observations for both foreground removal and avoidance methods. First, we calculate the 1D power spectra and compare the powers of radio halos with the EoR signal, which illustrates the impacts of radio halos with the foreground removal methods. Next, we calculate the 2D power spectra and carry out the comparison between radio halos and the EoR

signal inside the EoR window, from which we evaluate the effects imposed by radio halos in adopting the foreground avoidance methods to extract the EoR signal.

5.1. 1D Power Spectra

We calculate the 1D dimensionless power spectra $\Delta^2(k)$ for each image cube obtained in Section 3. For radio halos, we make use of all the 100 simulation runs (Section 2.1) to estimate the median power spectra and the corresponding 68% errors. The comparisons of the power spectra $\Delta^2(k)$ between radio halos and the EoR signal in each frequency band are displayed in Figure 6, where we also show the power spectra of Galactic diffuse emission and extragalactic point sources for comparison. The median power spectra (solid red lines) show that radio halos are generally more luminous than the EoR signal by about 4, 3, and 2 orders of magnitude on scales of $0.1 \text{ Mpc}^{-1} < k < 2 \text{ Mpc}^{-1}$ in the 120–128, 154–162, and 192–200 MHz bands, respectively. Given the large uncertainties in, e.g., brightness and number density, of radio halos, the power spectra can vary by about 10–100 times with respect to the median values within the 68% errors (red shaded regions). We also find that, although on large scales ($k \lesssim 0.1 \text{ Mpc}^{-1}$) the Galactic foreground is the strongest contaminating source, its power deceases rapidly as the scale becomes smaller and is weaker than the median power of radio halos by a factor of about 10–100 on scales of $0.5 \text{ Mpc}^{-1} \lesssim k \lesssim 1 \text{ Mpc}^{-1}$ in all the three bands. These results evidently show that radio halos are severe foreground contaminating sources. In addition, their diffuse and relatively complicated morphologies make it a challenge to accurately model and remove them.

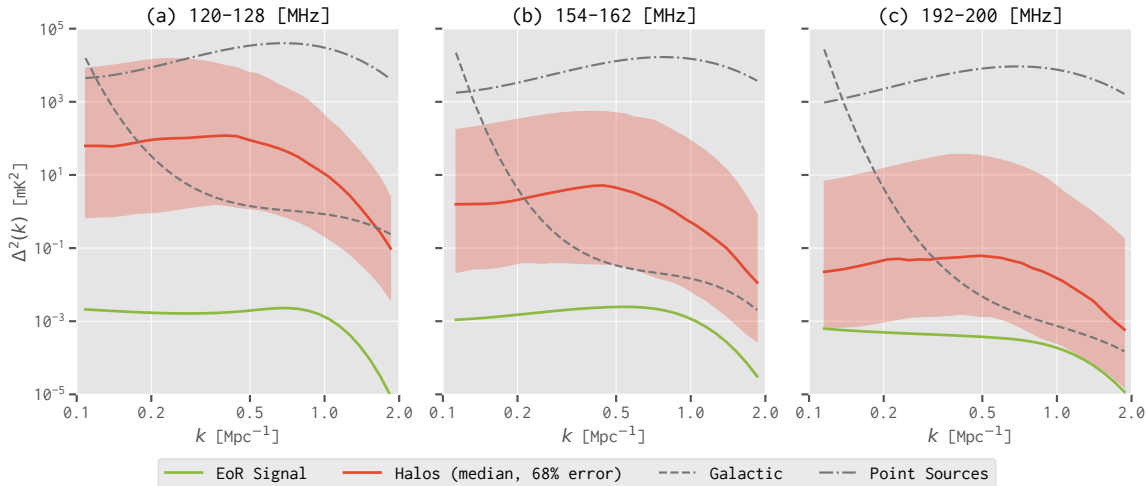


Figure 6. Comparisons of the 1D dimensionless power spectra $\Delta^2(k)$ among the EoR signal (the solid green line), radio halos (the solid red line), Galactic diffuse emission (the dashed gray line), and extragalactic point sources (the dash-dotted gray line) in the (a) 120–128 MHz, (b) 154–162 MHz, and (c) 192–200 MHz frequency bands. The solid red lines and shaded regions represent the median values and the corresponding 68% errors of the power spectra for radio halos estimated from the 100 simulation runs.

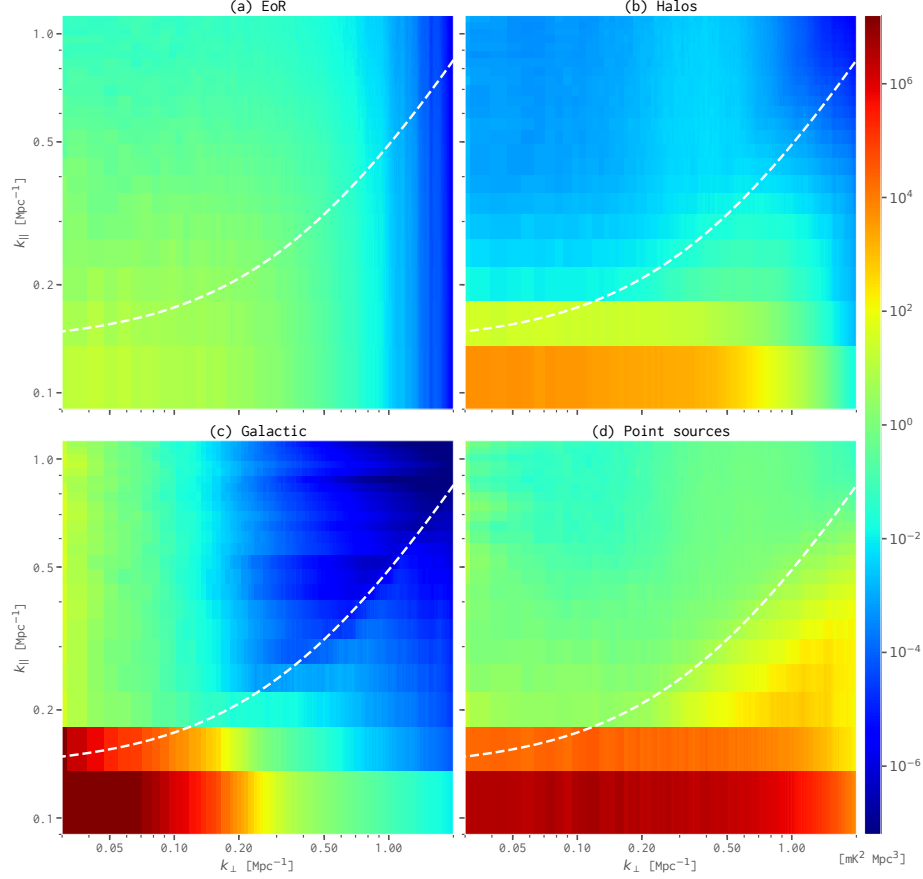


Figure 7. The 154–162 MHz 2D power spectra $P(k_\perp, k_\parallel)$ of (a) the EoR signal, (b) radio halos (median of the 100 simulation runs), (c) Galactic diffuse emission, and (d) extragalactic point sources. All panels share the same logarithmic scale in units of [mK 2 Mpc 3]. The dashed white lines mark the boundary between the EoR window (at the top left) and the contaminating wedge (at the bottom right).

5.2. 2D Power Spectra

In Figure 7 we take the 154–162 MHz band as an example to show the 2D power spectra $P(k_\perp, k_\parallel)$ of the EoR signal, radio halos (the median power spectrum of the 100 simulation runs), Galactic diffuse emission, and extragalactic point sources. We find that, as shown in many previous works, the EoR signal distributes its power across all k_\parallel modes, illustrating its rapid fluctuations along the line-of-sight dimension, while the spectral-smooth foreground components dominate only in the low- k_\parallel regions ($k_\parallel \lesssim 0.2$ Mpc $^{-1}$). With regard to the angular dimension, the power of radio halos appears in the range of $k_\perp \lesssim 1$ Mpc $^{-1}$, showing a concentration on the intermediate scales of $k_\perp \sim 0.5$ Mpc $^{-1}$. Meanwhile, the powers of Galactic diffuse emission and extragalactic point sources dominate on the larger scales of $k_\perp \lesssim 0.1$ Mpc $^{-1}$ and a broader angular scales of $k_\perp \gtrsim 0.1$ Mpc $^{-1}$, respectively. These results are also consistent with Figure 6(b).

In order to better evaluate the importance of radio halos as foreground contaminating sources, we calculate the 2D power spectrum ratios $R(k_\perp, k_\parallel)$ that are obtained

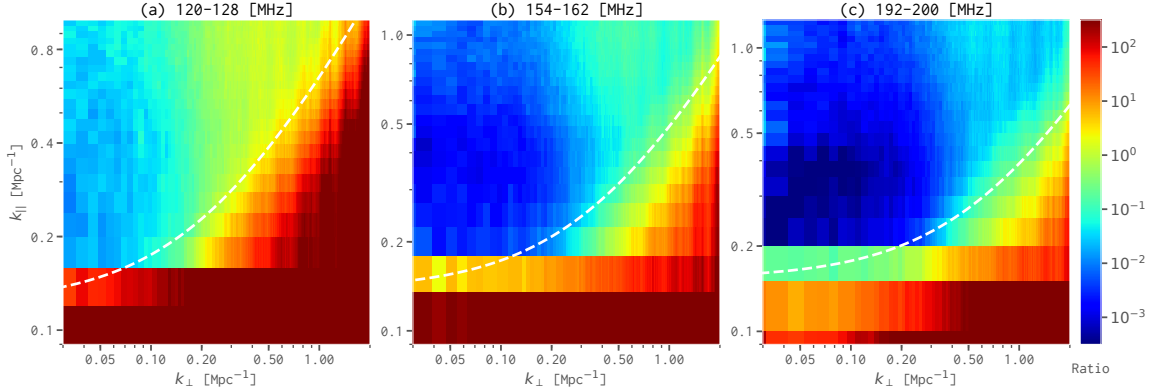


Figure 8. 2D power spectrum ratios $R(k_{\perp}, k_{\parallel})$ of radio halos to the EoR signal in the (a) 120–128 MHz, (b) 154–162 MHz, and (c) 192–200 MHz frequency bands. The median 2D power spectrum of 100 simulation runs for radio halos is used. All panels use the same color bar in logarithmic scale. The dashed white lines mark the EoR window boundaries.

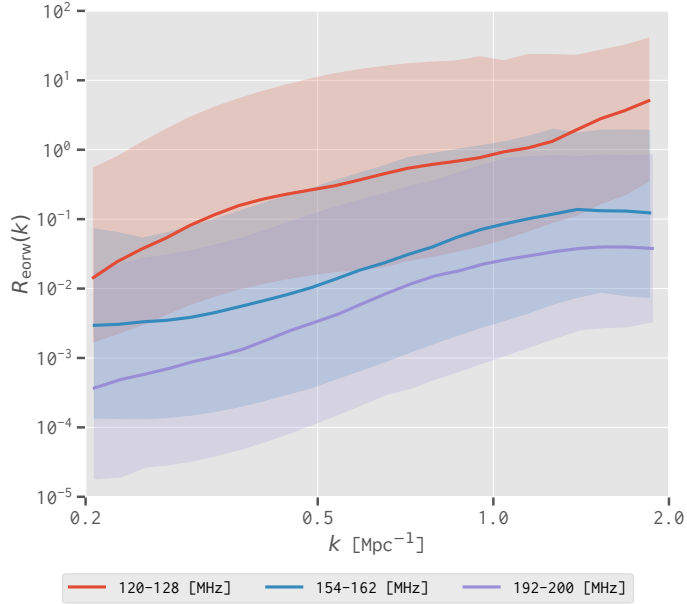


Figure 9. 1D power ratios $R_{\text{eorw}}(k)$ inside the EoR window of radio halos to the EoR signal. The solid lines and shaded regions show the median values and corresponding 68 % errors, respectively.

by dividing the median 2D power spectra of radio halos by those of the EoR signal in each frequency band. We find that, as shown in Figure 8, the EoR measurements will be significantly affected by radio halos on angular scales of $\gtrsim 0.1 \text{ Mpc}^{-1}$, $\gtrsim 0.3 \text{ Mpc}^{-1}$, and $\gtrsim 0.5 \text{ Mpc}^{-1}$ in the 120–128, 154–162, and 192–200 MHz bands, respectively. It is also clearly shown that radio halos turn to cause stronger contamination at lower frequencies ($\sim 120 \text{ MHz}$) than at higher frequencies ($\sim 200 \text{ MHz}$).

To further quantify the contamination caused by radio halos when foreground avoidance methods are applied, we need to appropriately define an EoR window in the $(k_{\perp}, k_{\parallel})$ plane to avoid the heavily contaminated areas and then compare the powers

of radio halos and the EoR signal derived inside the window. We have tested multiple parameter configurations (e, Θ) as defined in Equation (27), and find that when $e = 3$ and Θ that is about 3 times the radius of SKA1-Low's FoV (i.e., $\Theta = 7.5^\circ, 6.0^\circ$, and 4.8° in 120–128, 154–162, and 192–200 MHz, respectively) are used, a conservative EoR window boundary can be defined to effectively avoid the contaminating wedge (Figures 7 and 8). However, a significant part (about 55 %, 54 %, and 40 % in the 120–128, 154–162, and 192–200 MHz bands, respectively) of the power of the EoR signal is lost by adopting such EoR window boundaries. By averaging the modes only inside the defined EoR window, we calculate the 1D power spectrum ratios $R_{\text{eow}}(k)$ of radio halos to the EoR signal and present the results in Figure 9. We find that, on the scales of $0.5 \text{ Mpc}^{-1} \lesssim k \lesssim 1 \text{ Mpc}^{-1}$, the 1D power ratios can be up to about 10–20 in 120–128 MHz, 0.3–1 in 154–162 MHz, and 0.1–0.8 in 192–200 MHz within the 68 % errors (shaded regions).

Based on the above results, we conclude that radio halos are severe foreground contaminating sources to the EoR observations at ~ 200 MHz and become much stronger contaminating sources at ~ 120 MHz. Even if inside the EoR window where most of the strong foreground contamination is effectively avoided, radio halos can still imprint non-negligible contamination on the EoR measurements, especially at lower frequencies (~ 120 MHz).

6. DISCUSSIONS

In practical observations with low-frequency radio interferometers, the situations are much more complicated than our simulations. For example, calibration uncertainties (e.g., insufficient sky modeling) as well as other complicated instrumental and observational effects (e.g., cable signal reflections, ionospheric distortions) can cause frequency artifacts in the derived image cubes. Foreground sources located in the side-lobes of the station beam can also significantly reduce the imaging dynamical range and quality. In this section, we investigate how the EoR measurements are affected in these two situations if the contamination of radio halos is not properly removed.

6.1. Impacts of Frequency Artifacts

The smoothness along the frequency dimension is the most crucial feature of various foreground components and is the key to extract the faint EoR signal. However, frequency artifacts may present in the obtained image cubes due to calibration uncertainties and various instrumental and observational effects, which break the spectral smoothness of the foreground emission and hence damage the EoR measurements.

To evaluate the influence of the frequency artifacts on the power spectra, we multiply each slice of the image cube by a random number drawn from a Gaussian distribution with unity mean and then compare the resulting power spectra (Chapman et al. 2016). Some simulation and observation studies have suggested that the residual calibration errors in frequency channels may be about 0.1 %–1 % (e.g., Barry et al.

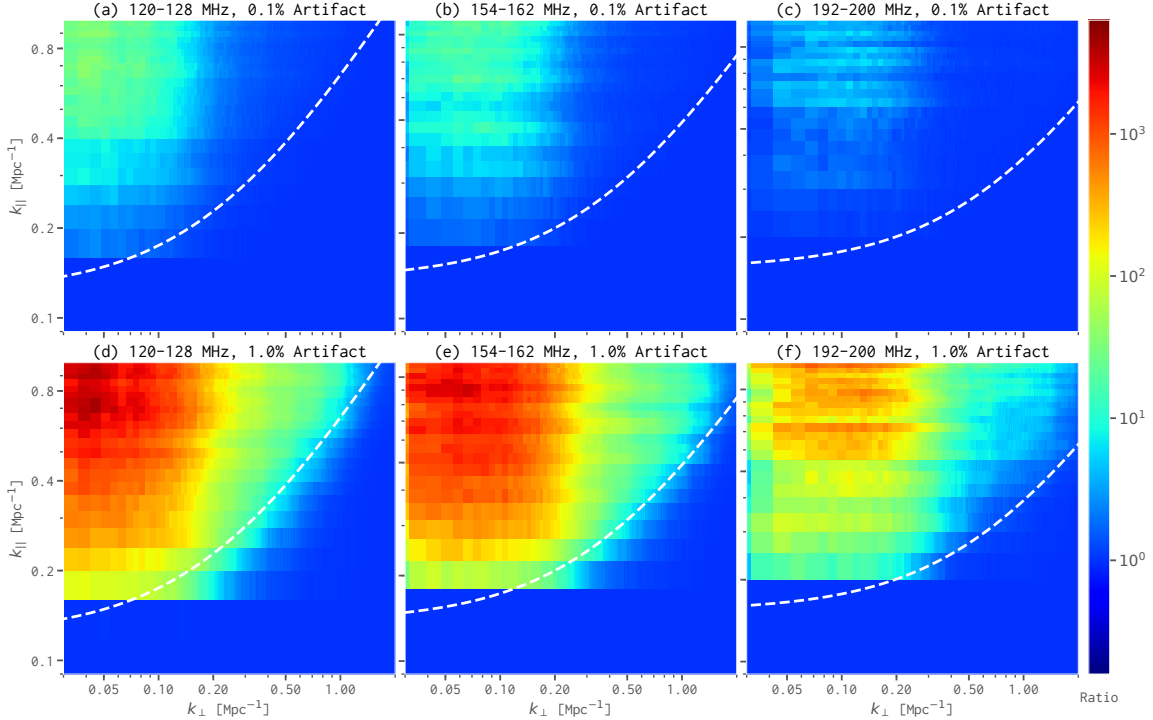


Figure 10. 2D power spectrum ratios $R_{\text{arti}}(k_{\perp}, k_{\parallel})$ of radio halos that are obtained between the modified image cubes with frequency artifacts and the original ones. All the 100 simulation runs for radio halos are used to derive the median 2D power spectrum ratios that are presented here. The top and bottom rows show the cases of frequency artifacts being $A_{\text{arti}} = 0.1\%$ and $A_{\text{arti}} = 1\%$, respectively. The left, middle, and right columns show the power spectrum ratios in the 120–128, 154–162, and 192–200 MHz bands, respectively. The dashed white lines mark the EoR window boundaries. All panels share the same color bar in logarithmic scale.

2016; Beardsley *et al.* 2016; Ewall-Wice *et al.* 2017). We thus investigate two extreme cases here: a frequency artifact of amplitude $A_{\text{arti}} = 0.1\%$ by using $\sigma = 0.001$ for the Gaussian distribution, and a frequency artifact of $A_{\text{arti}} = 1\%$ with $\sigma = 0.01$.

For each of the 100 simulation runs for radio halos, we calculate the 2D power spectrum ratios $R_{\text{arti}}(k_{\perp}, k_{\parallel})$ of the modified image cube with the frequency artifact to the original one (Section 3), and present the median 2D power spectrum ratios obtained in the 120–128, 154–162, and 192–200 MHz bands with either $A_{\text{arti}} = 0.1\%$ or 1% in Figure 10. We find that, when the frequency artifact is added, the resulting 2D power spectra are seriously damaged in all three frequency bands. On scales of $k_{\perp} \lesssim 0.2 \text{ Mpc}^{-1}$ and $k_{\parallel} \gtrsim 0.2 \text{ Mpc}^{-1}$, adding frequency artifact of $A_{\text{arti}} = 0.1\%$ causes the power of radio halos to be about 20, 10, and 3 times stronger in the 120–128, 154–162, and 192–200 MHz bands, respectively, and the corresponding power increases are about 2000, 1000, and 200 times for frequency artifact of $A_{\text{arti}} = 1\%$. As a comparison, we add the same frequency artifacts ($A_{\text{arti}} = 0.1\%$ and 1%) to the image cubes of the EoR signal, but find that the changes in the calculated 2D power spectra are negligible. This is because that the EoR signal already fluctuates remarkably along the frequency dimension. Therefore, even very minor ($\sim 0.1\%$) in-

strumental or calibration uncertainties can make the contamination of radio halos become much stronger, especially inside the EoR window. These results further support our conclusion made in Section 5.2 that radio halos are important foreground sources and must be carefully dealt with in EoR experiments.

6.2. Impacts of Far Side-lobes

Phased arrays, which are widely used in low-frequency radio interferometers (e.g., LOFAR, MWA, SKA1-Low), usually have complicated beam profiles. Sources far from the main lobe of the station beam can introduce noise-like corruptions, known as the far side-lobe confusion noise (FSCN; Smirnov et al. 2012), to images through the multitude of side-lobes. FSCN will not decrease once the uv coverage of the observation no longer improves, and can be the limiting factor in the noise performance of interferometers (Mort et al. 2017).

To investigate the impacts of FSCN contributed by the radio halos located in the far side-lobes of the station beam, we have generated the corresponding sky model for the **OSKAR** simulator, which evaluates the radio interferometer measurement equation (Smirnov 2011) and is able to perform full-sky simulations with realistic beam profiles. More details about the beam shapes and side-lobe properties of the SKA1-Low can be found in Mort et al. (2017). As an example, we simulate the radio halos in the 154–162 MHz band that cover the sky from the edge of the second side-lobe ($\phi \sim 10^\circ$ from the field center) to the horizon ($\phi = 90^\circ$). This emulates an ideal CLEAN procedure in practical data analysis that removes all the radio halos in both the main lobe and the first side-lobe but leaves the ones in the far side-lobes. Using the **OSKAR** simulator and the **WSClean** imager as described in Section 3, we obtain the dirty images of the central $5^\circ \times 5^\circ$ region and then calculate the 2D power spectrum.

From the 2D power spectrum shown in Figure 11(a), we find that the FSCN contributed by radio halos is remarkably strong, and the wedge-shaped contamination region moves toward the top left in the (k_\perp, k_\parallel) plane, which greatly reduces the EoR window. In order to effectively avoid the FSCN contamination, we are forced to employ a very conservative EoR window boundary, such as the one defined with $\Theta = 90^\circ$ as marked in Figure 11 with solid white line, at the cost of losing more information of the EoR signal. In Figure 11(b), we present the 2D power spectrum ratio of the FSCN to the EoR signal to better illustrate the impact of the FSCN on the EoR detection. It shows that even inside the newly defined EoR window ($\Theta = 90^\circ$), the FSCN resulted from radio halos can be about 1000 times stronger than the EoR signal on scales of $k_\perp \lesssim 0.1 \text{ Mpc}^{-1}$ and $k_\parallel \gtrsim 0.6 \text{ Mpc}^{-1}$. Consequently, the serious FSCN contamination makes the selection of EoR sky region a more challenging task, since in principle neither bright radio halos nor other strong sources are allowed in both the main and side lobes. A highly accurate foreground model is hence crucial to mitigate the impacts of FSCN.

7. SUMMARY

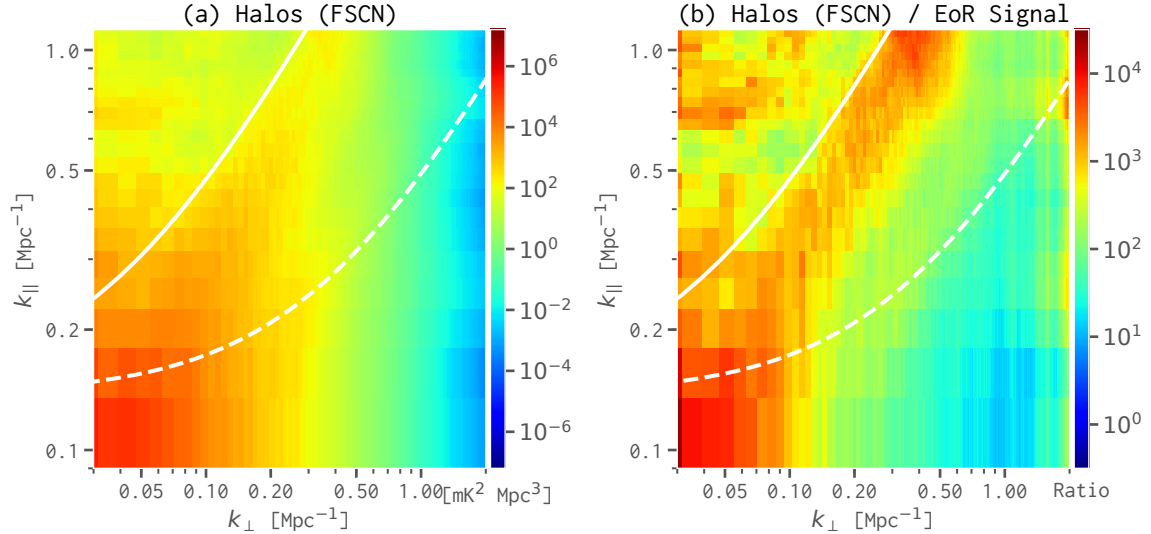


Figure 11. (a) The 2D power spectrum of the FSCN caused by radio halos in the far side-lobes of the station beam. (b) The 2D power spectrum ratio of the FSCN to the EoR signal. The results are derived in the 154–162 MHz band. The dashed and solid white lines mark the EoR window boundaries defined with $\Theta = 6^\circ$ and 90° , respectively.

Based on the Press-Schechter formalism and turbulence re-acceleration model, we have simulated the emission maps of radio halos, for which we have incorporated the SKA1-Low’s instrumental effects by utilizing the latest SKA1-Low layout configuration. By carrying out detailed comparisons of power spectra between radio halos and the EoR signal as well as the Galactic diffuse emission and extragalactic point sources in the 120–128, 154–162, and 192–200 MHz bands, we have shown that radio halos are severe contaminating sources, especially toward lower frequencies (~ 120 MHz). Even if inside the properly defined EoR windows, radio halos can still be non-negligible contaminating sources to the EoR observations. In addition, we have investigated the contamination resulted from frequency artifacts and radio halos located inside the far side-lobes, both of which support our conclusion that radio halos are severe foreground contaminating sources and need careful treatments in the forthcoming deep EoR observations.

We would like to thank Fred Dulwich for providing with the latest SKA1-Low layout configuration as well as the guidance on using the `OSKAR` simulator, André Offringa for the help on interferometric imaging with `WSClean`, Mathieu Remazeilles for providing us with the high-resolution Haslam 408 MHz Galactic synchrotron map, and Giovanna Giardino for the all-sky Galactic synchrotron spectral index map. We also acknowledge Emma Chapman, Uri Keshet, and Abhirup Datta for their help. Part of the work involving `OSKAR` and `WSClean` was performed on the high-performance cluster at Shanghai Astronomical Observatory, Chinese Academy of Sciences. This work is supported by the Ministry of Science and Technology of China (grant No. 2018YFA0404601), the National Natural Science Foundation of China (grant Nos.

11433002, 11621303, 61371147), and the National Key Research and Discovery Plan (grant No. 2017YFF0210903).

Software: OSKAR (Mort et al. 2010), WSClean (Offringa et al. 2014), AstroPy (Astropy Collaboration et al. 2013), HEALPix (Górski et al. 2005), HMF (Murray et al. 2013), IPython (<https://ipython.org/>), Matplotlib (<https://matplotlib.org/>), NumPy (<http://www.numpy.org/>), SciPy(<https://scipy.org/>), Pandas(<https://pandas.pydata.org/>).

APPENDIX

A. COLLECTION OF CURRENT OBSERVED RADIO HALOS

Table A1. Currently Observed 71 Radio Halos and 9 Candidates (As of 2018 January)

Cluster	Redshift	kpc//''	Size (Mpc)	$S_{1.4\text{ GHz}}$ (mJy)	$P_{1.4\text{ GHz}}$ (10^{24} W Hz^{-1})	Notes	References
(1)	(2)	(3)	(4)	(5)	(6)	(7)	(8)
1E 0657-56	0.2960	4.38	1.48	78.0 ± 5.0	21.33 ± 1.49		Liang et al. (2000)
Abell 141	0.2300	3.64	1.20	$1.3 \pm 0.1^{\text{a}}$	0.25 ± 0.02		Duchesne et al. (2017)
Abell 209	0.2060	3.34	1.40	16.9 ± 1.0	2.04 ± 0.12		Giovannini et al. (2009)
Abell 399	0.0718	1.35	0.57	16.0 ± 2.0	0.20 ± 0.03	With a relic candidate	Murgia et al. (2010)
Abell 401	0.0737	1.38	0.49	17.0 ± 1.0	0.20 ± 0.01	Double with Abell 401	Bacchi et al. (2003)
Abell 520	0.1990	3.25	0.99	34.4 ± 1.5	3.17 ± 0.14	Double with Abell 399	Govoni et al. (2001)
Abell 521	0.2533	3.91	1.17	5.9 ± 0.5	1.12 ± 0.09		Giovannini et al. (2009)
Abell 523	0.1000	1.82	1.30	59.0 ± 5.0	1.47 ± 0.12		Giovannini et al. (2011)
Abell 545	0.1540	2.64	0.81	23.0 ± 1.0	1.25 ± 0.05		Bacchi et al. (2003)
Abell 665	0.1818	3.03	1.66	43.1 ± 2.2	3.28 ± 0.17		Giovannini & Feretti (2000)
Abell 697	0.2820	4.23	0.75	5.2 ± 0.5	2.20 ± 0.21		van Weeren et al. (2011)
Abell 746	0.2320	3.67	0.85	18.0 ± 4.0	3.80 ± 0.84	With a relic	van Weeren et al. (2011)
Abell 754	0.0542	1.04	0.95	86.0 ± 4.0	0.56 ± 0.03	With a relic	Bacchi et al. (2003)
Abell 773	0.2170	3.48	1.13	12.7 ± 1.3	1.39 ± 0.14		Govoni et al. (2001)
Abell 781	0.3004	4.42	1.60	20.5 ± 5.0	5.90 ± 1.44	With a relic candidate	Govoni et al. (2011)
Abell 800	0.2223	3.55	1.28	10.6 ± 0.9	1.52 ± 0.13		Govoni et al. (2012)
Abell 851	0.4069	5.40	1.08	3.7 ± 0.3	2.14 ± 0.17		Giovannini et al. (2009)
Abell 1132	0.1369	2.39	0.74	3.3 ± 1.5	0.16 ± 0.07		Wilber et al. (2018)
Abell 1213	0.0469	0.91	0.22	72.2 ± 3.5	0.36 ± 0.02		Giovannini et al. (2009)
Abell 1300	0.3100	4.52	0.92	20.0 ± 2.0	2.99 ± 0.30	With a relic	Reid et al. (1999)
Abell 1351	0.3220	4.64	1.08	$32.4 \pm —$	$11.37 \pm —$		Giacintucci et al. (2009b)
Abell 1443	0.2700	4.10	1.10	$11.0 \pm 1.1^{\text{b}}$	2.53 ± 0.30	Halo candidate	Bonafede et al. (2015)
Abell 1451	0.1989	3.25	0.74	5.4 ± 0.5	0.62 ± 0.07	With a relic candidate	Cuciti et al. (2018)

Table A1 continued on next page

Table A1 (*continued*)

Cluster	Redshift	kpc/''	Size (Mpc)	$S_{1.4\text{ GHz}}$ (mJy)	$P_{1.4\text{ GHz}}$ (10^{24} W Hz^{-1})	Notes	References
(1)	(2)	(3)	(4)	(5)	(6)	(7)	(8)
Abell 1550	0.2540	3.92	1.41	7.7 ± 1.6	1.49 ± 0.31		Govoni et al. (2012)
Abell 1656	0.0232	0.46	0.58	530.0 ± 50.0	0.31 ± 0.03	With a relic candidate	Kim et al. (1990)
Abell 1682	0.2272	3.61	0.85	2.3 ± 0.5 ^e	0.41 ± 0.08	Halo candidate	Macario et al. (2013)
Abell 1689	0.1832	3.05	0.73	10.0 ± 2.9	0.92 ± 0.27		Vaccà et al. (2011)
Abell 1758A	0.2790	4.20	0.63	3.9 ± 0.4	0.93 ± 0.10	With a relic	Giovannini et al. (2009)
Abell 1914	0.1712	2.88	1.16	64.0 ± 3.0	4.32 ± 0.20		Bacchi et al. (2003)
Abell 1995	0.3186	4.61	0.83	4.1 ± 0.7	1.35 ± 0.23		Giovannini et al. (2009)
Abell 2034	0.1130	2.03	0.60	7.3 ± 2.0	0.28 ± 0.08	With a relic	van Weeren et al. (2011)
Abell 2061	0.0784	1.46	1.68	16.9 ± 4.2	0.25 ± 0.06	With a relic	Farnsworth et al. (2013)
Abell 2065	0.0726	1.36	1.08	32.9 ± 11.0	0.41 ± 0.14		Farnsworth et al. (2013)
Abell 2069	0.1160	2.08	0.90	6.2 ± 2.2 ^d	0.25 ± 0.05	Halo may have two components	Drabent et al. (2015)
Abell 2142	0.0909	1.67	0.99	11.8 ± 0.8	1.12 ± 0.08	Halo has two components	Venturi et al. (2017)
Abell 2163	0.2030	3.31	2.04	155.0 ± 2.0	14.93 ± 0.20	With a relic	Feretti et al. (2001)
Abell 2218	0.1710	2.88	0.35	4.7 ± 0.1	0.32 ± 0.01		Giovannini & Feretti (2000)
Abell 2219	0.2256	3.59	1.54	81.0 ± 4.0	9.72 ± 0.48		Bacchi et al. (2003)
Abell 2254	0.1780	2.98	0.85	33.7 ± 1.8	2.43 ± 0.13		Govoni et al. (2001)
Abell 2255	0.0806	1.50	0.90	56.0 ± 3.0	0.87 ± 0.05	With a relic	Govoni et al. (2005)
Abell 2256	0.0594	1.13	0.81	103.4 ± 1.1	0.82 ± 0.01		Clarke & Ensslin (2006)
Abell 2294	0.1780	2.98	0.54	5.8 ± 0.5	0.51 ± 0.04		Giovannini et al. (2009)
Abell 2319	0.0524	1.01	0.93	153.0 ± 8.0	0.54 ± 0.03		Feretti et al. (1997)
Abell 2680	0.1901	3.14	0.57	1.8 ± 0.6 ^e	0.16 ± 0.05	Halo candidate	Duchesne et al. (2017)
Abell 2693	0.1730	2.91	0.65	7.7 ± 0.9 ^f	0.61 ± 0.07	Halo candidate	Duchesne et al. (2017)
Abell 2744	0.3080	4.50	1.62	57.1 ± 2.9	12.89 ± 0.65	With a relic	Govoni et al. (2001)
Abell 2811	0.1080	1.95	0.48	3.4 ± 0.7 ^g	0.10 ± 0.02		Duchesne et al. (2017)
Abell 3411	0.1687	2.85	0.90	4.8 ± 0.5	0.46 ± 0.05	With a relic	van Weeren et al. (2013)
Abell 3562	0.0480	0.93	0.44	20.0 ± 2.0	0.10 ± 0.01		Venturi et al. (2003)

Table A1 continued on next page

Table A1 (*continued*)

Cluster	Redshift	kpc/''	Size (Mpc)	$S_{1.4\text{ GHz}}$ (mJy)	$P_{1.4\text{ GHz}}$ (10^{24} W Hz^{-1})	Notes	References
(1)	(2)	(3)	(4)	(5)	(6)	(7)	(8)
Abell 3888	0.1510	2.60	0.99	27.6 ± 3.1	1.85 ± 0.19		Shakouri et al. (2016)
Abell S84	0.1080	1.95	0.49	2.1 ± 0.3 ^h	0.06 ± 0.01	Halo candidate	Duchesne et al. (2017)
Abell S1121	0.3580	4.98	1.25	9.8 ± 3.1 ^h	4.54 ± 1.44		Duchesne et al. (2017)
ACT-CL J0102-4915	0.8700	7.73	2.17	10.7 ± 1.1 ⁱ	44.43 ± 1.28	With double relics	Lindner et al. (2014)
ACT-CL J0256.5+0006	0.3430	4.84	0.79	2.1 ± 0.5 ⁱ	0.97 ± 0.29		Knowles et al. (2016)
CIZA J0107.7+5408	0.1066	1.93	1.10	55.0 ± 5.0	1.80 ± 0.16		van Weeren et al. (2011)
CIZA J0638.1+4747	0.1740	2.92	0.59	3.6 ± 0.2	0.30 ± 0.02		Cuciti et al. (2018)
CIZA J1938.3+5409	0.2600	3.99	0.72	1.6 ± 0.2 ^b	0.36 ± 0.05		Bonafede et al. (2015)
CIZA J2242.8+5301	0.1921	3.16	1.77	33.5 ± 6.2 ^j	3.40 ± 0.97	With double relics	Govoni et al. (2012)
ClG 0016+16	0.5456	6.37	0.77	5.5 ± —	4.42 ± —		Giovannini & Feretti (2000)
ClG 0217+70	0.0655	1.24	0.73	58.6 ± 0.9	0.54 ± 0.01	With double relics	Brown et al. (2011)
ClG 1446+26	0.3700	5.09	1.22	7.7 ± 2.6	3.57 ± 1.21	With a relic	Govoni et al. (2012)
ClG 1821+64	0.2990	4.41	1.10	13.0 ± 0.8 ^k	3.70 ± 0.10		Bonafede et al. (2014b)
MACS J0416.1-2403	0.3960	5.31	0.64	1.7 ± 0.8 ^l	1.26 ± 0.29		Pandey-Pommier et al. (2015)
MACS J0520.7-1328	0.3400	4.81	0.80	9.0 ± 1.6	3.38 ± 0.60	Halo candidate	Macario et al. (2014)
MACS J0553.4-3342	0.4070	5.40	1.32	9.2 ± 0.7 ^b	6.73 ± 0.61		Bonafede et al. (2012)
MACS J0717.5+3745	0.5458	6.37	1.20	118.0 ± 5.0	50.00 ± 10.00	With a relic	van Weeren et al. (2009)
MACS J0949.8+1708	0.3825	5.20	1.04	3.1 ± 0.3 ^b	1.63 ± 0.15		Bonafede et al. (2015)
MACS J1149.5+2223	0.5444	6.36	1.32	1.2 ± 0.5	1.95 ± 0.93	Halo candidate; with double relics	Bonafede et al. (2012)
MACS J1752.0+4440	0.3660	5.05	1.65	14.2 ± 1.4 ^m	9.50 ± 0.91	With double relics	van Weeren et al. (2012)
MACS J2243.3-0935	0.4470	5.71	0.91	3.1 ± 0.6 ⁿ	3.11 ± 0.58	With a relic candidate	Cantwell et al. (2016)
PLCK G147.3-16.6	0.6500	6.92	1.80	2.5 ± 0.4 ^o	5.10 ± 0.80		van Weeren et al. (2014)
PLCK G171.9-40.7	0.2700	4.10	0.99	18.0 ± 2.0	4.76 ± 0.10		Giacintucci et al. (2013)
PLCK G285.0-23.7	0.3900	5.26	0.73	2.9 ± 0.4 ^p	1.67 ± 0.21		Martinez Aviles et al. (2016)
PLCK G287.0+32.9	0.3900	5.26	1.30	8.8 ± 0.9	5.10 ± 0.51	With double relics	Bonafede et al. (2014a)
PSZ1 G108.18-11.53	0.3347	4.77	0.84	6.8 ± 0.2	2.72 ± 0.10	With double relics	de Gasperin et al. (2015)

Table A1 continued on next page

Table A1 (*continued*)

Cluster	Redshift	kpc/''	Size (Mpc)	$S_{1.4\text{ GHz}}$ (mJy)	$P_{1.4\text{ GHz}}$ (10^{24} W Hz^{-1})	Notes (7)	References (8)
(1)	(2)	(3)	(4)	(5)	(6)		
RXC J1234.2+0947	0.2290	3.63	0.92	2.0 ± —	0.30 ± —	Halo candidate	Govoni et al. (2012)
RXC J1314.4–2515	0.2474	3.85	1.27	20.3 ± 0.8	1.45 ± 0.06	With double relics	Feretti et al. (2005)
RXC J1514.9–1523	0.2226	3.55	1.38	10.0 ± 2.0	1.65 ± 0.33		Giacintucci et al. (2011)
RXC J2003.5–2323	0.3171	4.59	1.38	35.0 ± 2.0	11.96 ± 0.68		Giacintucci et al. (2009a)
RXC J2351.0–1954	0.2477	3.85	0.64	4.5 ± 0.9 ^q	0.89 ± 0.18	Halo candidate	Duchesne et al. (2017)

Table A1 continued on next page

Table A1 (*continued*)

Cluster:	Redshift	kpc/''	Size (Mpc)	$S_{1.4\text{ GHz}}$ (mJy)	$P_{1.4\text{ GHz}}$ (10^{24} W Hz^{-1})	Notes	References
(1)	(2)	(3)	(4)	(5)	(6)	(7)	(8)

a Extrapolated from 168 MHz with spectral index $\alpha = 2.1$.*b* Extrapolated from 323 MHz with spectral index $\alpha = 1.3$.*c* Extrapolated from 153 MHz with spectral index $\alpha = 1.7$.*d* Extrapolated from 346 MHz with spectral index $\alpha = 1.0$.*e* Extrapolated from 168 MHz with spectral index $\alpha = 1.2$.*f* Extrapolated from 168 MHz with spectral index $\alpha = 0.88$.*g* Extrapolated from 168 MHz with spectral index $\alpha = 1.5$.*h* Extrapolated from 168 MHz with spectral index $\alpha = 1.3$.*i* Extrapolated from 610 MHz with spectral index $\alpha = 1.2$.*j* Extrapolated from 145 MHz with spectral index $\alpha = 1.03$.*k* Extrapolated from 325 MHz with spectral index $\alpha = 1.04$.*l* Extrapolated from 340 MHz with spectral index $\alpha = 1.5$.*m* Extrapolated from 1714 MHz with spectral index $\alpha = 1.1$.*n* Extrapolated from 610 MHz with spectral index $\alpha = 1.4$.*p* Extrapolated from 1867 MHz with spectral index $\alpha = 1.3$.*q* Extrapolated from 168 MHz with spectral index $\alpha = 1.4$.

NOTE—Columns: (1) galaxy cluster name; (2) redshift; (3) kpc per arcsec at the cluster's redshift (converted to our adopted cosmology); (4) largest linear size of the radio halo, in units of Mpc; (5) 1.4 GHz flux density; (6) 1.4 GHz radio power (converted to our adopted cosmology); (7) additional notes; (8) references to the quoted properties.

B. SUPPLEMENTAL FORMULAS

In a flat Λ CDM cosmology as adopted in this work, the critical linear overdensity as a function of redshift z is (Kitayama & Suto 1996; Randall et al. 2002)

$$\delta_c(z) = \frac{D(z=0)}{D(z)} \frac{3}{20} (12\pi)^{2/3} [1 + 0.0123 \log_{10} \Omega_f(z)], \quad (\text{B1})$$

where $\Omega_f(z)$ is the mass density ratio at redshift z defined as

$$\Omega_f(z) = \frac{\Omega_m(1+z)^3}{\Omega_m(1+z)^3 + \Omega_\Lambda}, \quad (\text{B2})$$

and $D(z)$ is the growth factor given by (Peebles 1980, equation (13.6))

$$D(x) = \frac{(x^3 + 2)^{1/2}}{x^{3/2}} \int_0^x y^{3/2} (y^3 + 2)^{-3/2} dy, \quad (\text{B3})$$

with $x_0 \equiv (2\Omega_\Lambda/\Omega_m)^{1/3}$ and $x = x_0/(1+z)$.

The Hubble parameter at redshift z is

$$H(z) = H_0 E(z) = H_0 \sqrt{\Omega_m(1+z)^3 + \Omega_\Lambda}, \quad (\text{B4})$$

where $E(z)$ is the redshift evolution factor (Hogg 1999).

The virial radius of a galaxy cluster is defined as

$$r_{\text{vir}} = \left[\frac{3M_{\text{vir}}}{4\pi \Delta_{\text{vir}}(z) \rho_{\text{crit}}(z)} \right]^{1/3}, \quad (\text{B5})$$

where M_{vir} is the virial mass of the cluster, $\rho_{\text{crit}}(z) = 3H^2(z)/(8\pi G)$ is the critical density at redshift z with G being the gravitational constant, and $\Delta_{\text{vir}}(z)$ is the average overdensity of the cluster given by (Kitayama & Suto 1996; Cassano & Brunetti 2005)

$$\Delta_{\text{vir}}(z) = 18\pi^2 [1 + 0.4093 w(z)^{0.9052}], \quad (\text{B6})$$

where $w(z) \equiv \Omega_f^{-1}(z) - 1$.

REFERENCES

- Astropy Collaboration, Robitaille, T. P., Tollerud, E. J., et al. 2013, *A&A*, **558**, A33
- Bacchi, M., Feretti, L., Giovannini, G., & Govoni, F. 2003, *A&A*, **400**, 465
- Barry, N., Hazelton, B., Sullivan, I., Morales, M. F., & Pober, J. C. 2016, *MNRAS*, **461**, 3135
- Beardsley, A. P., Hazelton, B. J., Sullivan, I. S., et al. 2016, *ApJ*, **833**, 102
- Blasi, P., Gabici, S., & Brunetti, G. 2007, *International Journal of Modern Physics A*, **22**, 681
- Böhringer, H., Chon, G., & Kronberg, P. P. 2016, *A&A*, **596**, A22
- Bonafede, A., Intema, H. T., Brüggen, M., et al. 2014a, *ApJ*, **785**, 1

- Bonafede, A., Brüggen, M., van Weeren, R., et al. 2012, *MNRAS*, **426**, 40
- Bonafede, A., Intema, H. T., Brüggen, M., et al. 2014b, *MNRAS*, **444**, L44
- Bonafede, A., Intema, H., Brüggen, M., et al. 2015, *MNRAS*, **454**, 3391
- Bond, J. R., Cole, S., Efstathiou, G., & Kaiser, N. 1991, *ApJ*, **379**, 440
- Bowman, J. D., Cairns, I., Kaplan, D. L., et al. 2013, *PASA*, **30**, e031
- Briggs, D. S. 1995, PhD thesis, The New Mexico Institute of Mining and Technology
- Brown, S., Duesterhoeft, J., & Rudnick, L. 2011, *ApJL*, **727**, L25
- Brunetti, G., Cassano, R., Dolag, K., & Setti, G. 2009, *A&A*, **507**, 661
- Brunetti, G., & Lazarian, A. 2007, *MNRAS*, **378**, 245
- . 2011, *MNRAS*, **410**, 127
- Cantwell, T. M., Scaife, A. M. M., Oozeer, N., Wen, Z. L., & Han, J. L. 2016, *MNRAS*, **458**, 1803
- Cassano, R., & Brunetti, G. 2005, *MNRAS*, **357**, 1313
- Cassano, R., Brunetti, G., Giocoli, C., & Ettori, S. 2016, *A&A*, **593**, A81
- Cassano, R., Bernardi, G., Brunetti, G., et al. 2015, *Advancing Astrophysics with the Square Kilometre Array (AASKA14)*, 73
- Chang, J. S., & Cooper, G. 1970, *Journal of Computational Physics*, **6**, 1
- Chapman, E., Zaroubi, S., Abdalla, F. B., et al. 2016, *MNRAS*, **458**, 2928
- Clarke, T. E., & Ensslin, T. A. 2006, *AJ*, **131**, 2900
- Cuciti, V., Brunetti, G., van Weeren, R., et al. 2018, *A&A*, **609**, A61
- Datta, A., Bowman, J. D., & Carilli, C. L. 2010, *ApJ*, **724**, 526
- de Gasperin, F., Intema, H. T., van Weeren, R. J., et al. 2015, *MNRAS*, **453**, 3483
- DeBoer, D. R., Parsons, A. R., Aguirre, J. E., et al. 2017, *PASP*, **129**, 045001
- Di Matteo, T., Ciardi, B., & Miniati, F. 2004, *MNRAS*, **355**, 1053
- Dickinson, C., Davies, R. D., & Davis, R. J. 2003, *MNRAS*, **341**, 369
- Donnert, J., & Brunetti, G. 2014, *MNRAS*, **443**, 3564
- Drabent, A., Hoeft, M., Pizzo, R. F., et al. 2015, *A&A*, **575**, A8
- Duchesne, S. W., Johnston-Hollitt, M., Offringa, A. R., et al. 2017, *ArXiv e-prints*, arXiv:1707.03517
- Eilek, J. A., & Hughes, P. A. 1991, Particle acceleration and magnetic field evolution, ed. P. A. Hughes (Cambridge University Press), 428
- Ettori, S., Donnarumma, A., Pointecouteau, E., et al. 2013, *SSRv*, **177**, 119
- Ewall-Wice, A., Dillon, J. S., Liu, A., & Hewitt, J. 2017, *MNRAS*, **470**, 1849
- Fan, X., Carilli, C. L., & Keating, B. 2006, *ARA&A*, **44**, 415
- Farnsworth, D., Rudnick, L., Brown, S., & Brunetti, G. 2013, *ApJ*, **779**, 189
- Feretti, L., Fusco-Femiano, R., Giovannini, G., & Govoni, F. 2001, *A&A*, **373**, 106
- Feretti, L., Giovannini, G., & Böhringer, H. 1997, *NewA*, **2**, 501
- Feretti, L., Giovannini, G., Govoni, F., & Murgia, M. 2012, *A&A Rev*, **20**, 54
- Feretti, L., Schuecker, P., Böhringer, H., Govoni, F., & Giovannini, G. 2005, *A&A*, **444**, 157
- Finkbeiner, D. P. 2003, *ApJS*, **146**, 407
- Furlanetto, S. R. 2016, Understanding the Epoch of Cosmic Reionization: Challenges and Progress, **423**, 247
- Furlanetto, S. R., Oh, S. P., & Briggs, F. H. 2006, *PhR*, **433**, 181
- Giacintucci, S., Dallacasa, D., Venturi, T., et al. 2011, *A&A*, **534**, A57
- Giacintucci, S., Kale, R., Wik, D. R., Venturi, T., & Markevitch, M. 2013, *ApJ*, **766**, 18
- Giacintucci, S., Venturi, T., Brunetti, G., et al. 2009a, *A&A*, **505**, 45
- Giacintucci, S., Venturi, T., Cassano, R., Dallacasa, D., & Brunetti, G. 2009b, *ApJL*, **704**, L54
- Giardino, G., Banday, A. J., Górski, K. M., et al. 2002, *A&A*, **387**, 82
- Giovannini, G., Bonafede, A., Feretti, L., et al. 2009, *A&A*, **507**, 1257

- Giovannini, G., & Feretti, L. 2000, *NewA*, 5, 335
- Giovannini, G., Feretti, L., Girardi, M., et al. 2011, *A&A*, 530, L5
- Gleser, L., Nusser, A., & Benson, A. J. 2008, *MNRAS*, 391, 383
- Górski, K. M., Hivon, E., Banday, A. J., et al. 2005, *ApJ*, 622, 759
- Govoni, F., Feretti, L., Giovannini, G., et al. 2001, *A&A*, 376, 803
- Govoni, F., Ferrari, C., Feretti, L., et al. 2012, *A&A*, 545, A74
- Govoni, F., Murgia, M., Feretti, L., et al. 2005, *A&A*, 430, L5
- Govoni, F., Murgia, M., Giovannini, G., Vacca, V., & Bonafede, A. 2011, *A&A*, 529, A69
- Hogg, D. W. 1999, ArXiv Astrophysics e-prints, astro-ph/9905116
- Intema, H. T., van der Tol, S., Cotton, W. D., et al. 2009, *A&A*, 501, 1185
- Jelić, V., Zaroubi, S., Labropoulos, P., et al. 2008, *MNRAS*, 389, 1319
- Keshet, U., Waxman, E., & Loeb, A. 2004, *NewAR*, 48, 1119
- Kim, K.-T., Kronberg, P. P., Dewdney, P. E., & Landecker, T. L. 1990, *ApJ*, 355, 29
- Kitayama, T., & Suto, Y. 1996, *ApJ*, 469, 480
- Knowles, K., Intema, H. T., Baker, A. J., et al. 2016, *MNRAS*, 459, 4240
- Koopmans, L., Pritchard, J., Mellema, G., et al. 2015, *Advancing Astrophysics with the Square Kilometre Array (AASKA14)*, 1
- Lacey, C., & Cole, S. 1993, *MNRAS*, 262, 627
- Large, M. I., Mathewson, D. S., & Haslam, C. G. T. 1959, *Nature*, 183, 1663
- Liang, H., Hunstead, R. W., Birkinshaw, M., & Andreani, P. 2000, *ApJ*, 544, 686
- Lindner, R. R., Baker, A. J., Hughes, J. P., et al. 2014, *ApJ*, 786, 49
- Liu, A., Parsons, A. R., & Trott, C. M. 2014, *PhRvD*, 90, 023018
- Liu, A., & Tegmark, M. 2012, *MNRAS*, 419, 3491
- Lokas, E. L., & Mamon, G. A. 2001, *MNRAS*, 321, 155
- Macario, G., Venturi, T., Intema, H. T., et al. 2013, *A&A*, 551, A141
- Macario, G., Intema, H. T., Ferrari, C., et al. 2014, *A&A*, 565, A13
- Martinez Aviles, G., Ferrari, C., Johnston-Hollitt, M., et al. 2016, *A&A*, 595, A116
- Mellema, G., Koopmans, L. V. E., Abdalla, F. A., et al. 2013, *Experimental Astronomy*, 36, 235
- Mesinger, A., Greig, B., & Sobacchi, E. 2016, *MNRAS*, 459, 2342
- Minati, F. 2015, *ApJ*, 800, 60
- Mitchell, D. A., Greenhill, L. J., Wayth, R. B., et al. 2008, *IEEE Journal of Selected Topics in Signal Processing*, 2, 707
- Morales, M. F., Bowman, J. D., Cappallo, R., Hewitt, J. N., & Lonsdale, C. J. 2006, *NewAR*, 50, 173
- Morales, M. F., Hazelton, B., Sullivan, I., & Beardsley, A. 2012, *ApJ*, 752, 137
- Morales, M. F., & Hewitt, J. 2004, *ApJ*, 615, 7
- Morales, M. F., & Wyithe, J. S. B. 2010, *ARA&A*, 48, 127
- Mort, B., Dulwich, F., Razavi-Ghods, N., de Lera Acedo, E., & Grainge, K. 2017, *MNRAS*, 465, 3680
- Mort, B. J., Dulwich, F., Salvini, S., Adami, K. Z., & Jones, M. E. 2010, in 2010 IEEE International Symposium on Phased Array Systems and Technology, 690–694
- Murgia, M., Govoni, F., Feretti, L., & Giovannini, G. 2010, *A&A*, 509, A86
- Murgia, M., Govoni, F., Markevitch, M., et al. 2009, *A&A*, 499, 679
- Murray, S. G., Power, C., & Robotham, A. S. G. 2013, *Astronomy and Computing*, 3, 23
- Murray, S. G., Trott, C. M., & Jordan, C. H. 2017, *ApJ*, 845, 7
- Navarro, J. F., Frenk, C. S., & White, S. D. M. 1997, *ApJ*, 490, 493
- Offringa, A. R., & Smirnov, O. 2017, *MNRAS*, 471, 301

- Offringa, A. R., McKinley, B., Hurley-Walker, N., et al. 2014, *MNRAS*, **444**, 606
- Pandey-Pommier, M., van Weeren, R. J., Ogrean, G. A., et al. 2015, in SF2A-2015: Proceedings of the Annual meeting of the French Society of Astronomy and Astrophysics, ed. F. Martins, S. Boissier, V. Buat, L. Cambrésy, & P. Petit, 247–252
- Park, B. T., & Petrosian, V. 1996, *ApJS*, **103**, 255
- Parsons, A. R., Backer, D. C., Foster, G. S., et al. 2010, *AJ*, **139**, 1468
- Peebles, P. J. E. 1980, The Large-scale Structure of the Universe (Princeton University Press)
- Pindor, B., Wyithe, J. S. B., Mitchell, D. A., et al. 2011, *PASA*, **28**, 46
- Pinzke, A., Oh, S. P., & Pfrommer, C. 2017, *MNRAS*, **465**, 4800
- Press, W. H., & Schechter, P. 1974, *ApJ*, **187**, 425
- Randall, S. W., Sarazin, C. L., & Ricker, P. M. 2002, *ApJ*, **577**, 579
- Reid, A. D., Hunstead, R. W., Lemonon, L., & Pierre, M. M. 1999, *MNRAS*, **302**, 571
- Remazeilles, M., Dickinson, C., Banday, A. J., Bigot-Sazy, M.-A., & Ghosh, T. 2015, *MNRAS*, **451**, 4311
- Rybicki, G. B., & Lightman, A. P. 1979, Radiative Processes in Astrophysics, A Wiley-Interscience publication (Wiley)
- Sarazin, C. L. 1999, *ApJ*, **520**, 529
- Sarazin, C. L. 2002, in Astrophysics and Space Science Library, Vol. 272, Merging Processes in Galaxy Clusters, ed. L. Feretti, I. M. Gioia, & G. Giovannini, 1–38
- Schlickeiser, R. 2002, Cosmic Ray Astrophysics (Springer)
- Shakouri, S., Johnston-Hollitt, M., & Pratt, G. W. 2016, *MNRAS*, **459**, 2525
- Shaver, P. A., Windhorst, R. A., Madau, P., & de Bruyn, A. G. 1999, *A&A*, **345**, 380
- Smirnov, O. M. 2011, *A&A*, **527**, A106
- Smirnov, O. M., Frank, B. S., Theron, I. P., & Wood, I. H. 2012, in 2012 International Conference on Electromagnetics in Advanced Applications, 586–590
- Spinelli, M., Bernardi, G., & Santos, M. G. 2018, *ArXiv e-prints*, arXiv:1802.03060
- Thyagarajan, N., Udaya Shankar, N., Subrahmanyam, R., et al. 2013, *ApJ*, **776**, 6
- Tingay, S. J., Goeke, R., Bowman, J. D., et al. 2013, *PASA*, **30**, e007
- Tormen, G., Moscardini, L., & Yoshida, N. 2004, *MNRAS*, **350**, 1397
- Trott, C. M., & Tingay, S. J. 2015, *ApJ*, **814**, 27
- Vacca, V., Govoni, F., Murgia, M., et al. 2011, *A&A*, **535**, A82
- van Haarlem, M. P., Wise, M. W., Gunst, A. W., et al. 2013, *A&A*, **556**, A2
- van Weeren, R. J., Bonafede, A., Ebeling, H., et al. 2012, *MNRAS*, **425**, L36
- van Weeren, R. J., Brüggen, M., Röttgering, H. J. A., et al. 2011, *A&A*, **533**, A35
- van Weeren, R. J., Röttgering, H. J. A., Brüggen, M., & Cohen, A. 2009, *A&A*, **505**, 991
- van Weeren, R. J., Fogarty, K., Jones, C., et al. 2013, *ApJ*, **769**, 101
- van Weeren, R. J., Intema, H. T., Lal, D. V., et al. 2014, *ApJL*, **781**, L32
- Vazza, F., Brunetti, G., Gheller, C., Brunino, R., & Brüggen, M. 2011, *A&A*, **529**, A17
- Vazza, F., Ferrari, C., Bonafede, A., et al. 2015, Advancing Astrophysics with the Square Kilometre Array (AASKA14), 97
- Venturi, T., Bardelli, S., Dallacasa, D., et al. 2003, *A&A*, **402**, 913
- Venturi, T., Rossetti, M., Brunetti, G., et al. 2017, *A&A*, **603**, A125
- Wang, J., Xu, H., Gu, J., et al. 2010, *ApJ*, **723**, 620
- Wang, J., Xu, H., An, T., et al. 2013, *ApJ*, **763**, 90
- Wilber, A., Brüggen, M., Bonafede, A., et al. 2018, *MNRAS*, **473**, 3536

- Wilman, R. J., Miller, L., Jarvis, M. J., et al. 2008, *MNRAS*, 388, 1335
- Wyithe, J. S. B., & Loeb, A. 2004, *Nature*, 432, 194
- Zaroubi, S. 2013, in *Astrophysics and Space Science Library*, Vol. 396, *The First Galaxies*, ed. T. Wiklind, B. Mobasher, & V. Bromm, 45
- Zheng, Q., Wu, X.-P., Johnston-Hollitt, M., Gu, J.-h., & Xu, H. 2016, *ApJ*, 832, 190